An isogeometric approach to topology optimization of multi-material and functionally graded structures

Alireza H. Taheri, Krishnan Suresh*

Department of Mechanical Engineering, UW-Madison, Madison, Wisconsin 53706, USA.

* Corresponding author, email: ksuresh@wisc.edu

Abstract

A new isogeometric density based approach for the topology optimization of multi-material structures is presented. In this method, the density fields of multiple material phases are represented using the isogeometric NURBS-based parameterization leading to exact modeling of the geometry, and removing numerical artifacts. Moreover, due to the unified parameterization of the geometry, analysis and design space, the sensitivities are computed analytically, and in a cost effective manner. An extension of the perimeter control technique is proposed where restrictions are imposed on the perimeters of density fields of all phases. Due to higher order continuity of the density fields, the gradients are calculated exactly without additional computational cost. Consequently, not only can mesh-independency be achieved, but the complexity of the optimal design can be controlled easily. The problem is formulated with constraints on either: (a) volume fractions of different material phases, or (b) the total mass of the structure. The proposed method is applied for the minimal compliance design of two-dimensional structures consisting of multiple distinct materials as well as functionally graded ones. Numerical results demonstrate high quality of the obtained optimal designs, and superior performance of these structures compared to the corresponding single material topological designs.

Keywords: isogeometric analysis, topology optimization, multi-materials, functionally graded materials, perimeter control.

1. Introduction

Improving the performance of structures has always been of great interest to the engineering community. Towards this end, different methods of structural optimization have been developed, namely, structural shape, size, topology and materials optimization. Among these strategies, structural topology optimization is the most widely used concept and is believed to yield the highest performance. However, the performance of topological designs could still be improved by using heterogeneous materials instead of the homogeneous ones. In this research, after reviewing the existing literature in this area, we will investigate the applicability of isogeometric analysis (IGA) method [1], specifically through a Non-uniform Rational B-spline (NURBS) parameterization within a density based optimization approach.

1.1. Multi-material topology optimization

In theory, most of the existing methods for single-material (solid-void) structural topology optimization could be extended towards multi-material optimization. However, compared with single-material design, multi-materials optimization poses additional challenges [2]. First, an appropriate topology description model which can effectively capture each distinct phase within the domain is required [2]. An ideal representation model should also have an explicit and continuous mathematical form to ease the sensitivity analysis. Moreover, in order to obtain realistic designs, overlaps between different phases should be avoided [2], unless functionally graded materials are desired. Finally, the method should be capable of handling any number of material phases and constraints in an efficient manner.

Owing to the advantage of yielding smooth boundaries and distinct interface between the material phases, the level-set based methods are gaining popularity [2–5]. However, this class of optimization methods usually lacks the critical ability to nucleate new holes in the design domain, and consequently the optimization result is typically dependent on the initial guess. Recently developed level set methods that allow for the nucleation of new holes are discussed in [6–8]. For a rigorous review on multi-material level-set topology optimization methods, the reader is referred to [2] and references therein.

The application of phase-field approaches for multi-material topology optimization of structures has been investigated in [9–12]. By employing multi-material phase-field approach based on

Cahn-Hilliard equation, a general method to solve multiphase structural topology optimization problems has been introduced by Zhou and Wang [9,10]. While the intrinsic volume preserving property is introduced as the main advantage of this method, that is, the iterations will be kept strictly feasible with respect to the design domain without any additional effort, the slow rate of convergence, especially in case of multiple materials, is the main drawback of this approach. Tavakoli and Mohseni [13] introduced an alternating active-phase algorithm which is based on the splitting of a multi-phase topology optimization problem into a series of binary phase sub-problems solved using a traditional binary topology optimization solver. The extension of bi-directional evolutionary optimization method for multi-material structures is proposed by Huang and Xie [14].

The solid isotropic material with penalization (SIMP) method, which is the subject of this study, is one of the other popular ideas for the topology optimization of multi-material structures. The performance of this class of optimization approaches depends highly on the representation method of the density field as well as the material interpolation schemes. Hence, significant research has been conducted on this subject and various techniques have been proposed thus far.

The extension of the SIMP method for multi-material topology optimization was first introduced by Sigmund and Torquato [15] where the method is applied for the design of materials with extreme thermal expansion. The method was later employed for the design of multi-physics actuators [16] and multiphase composites with extremal bulk modulus [17]. In 1999, Bendsoe and Sigmund [18] investigated the physical interpretation of the SIMP interpolation scheme in the light of variational bounds on the effective properties of composite materials. Despite proving that the so called artificial interpolation model employed in SIMP in many circumstances falls within the framework of microstructurally based models, their study shows that in case of multiphase materials the SIMP model will never satisfy the Hashin-Shtrikman bounds for all densities. However, it is possible to keep the SIMP model fairly close to the behavior governed by these bounds [18].

Several other material interpolation schemes for multi-material topology optimization have also been proposed. These include peak function [19], uniform multi-phase materials interpolation [20], generalizations of SIMP and rational approximation of material properties (RAMP)

schemes [20], and a family of discrete material optimization methods [22]. For a rigorous comparative study on these interpolation schemes, we refer to [21,22].

In one of the latest studies in this field, a multi-resolution implementation in 3D for multi-material topology optimization problem is proposed by Park and Sutradhar [23]. The method employs an alternating active-phase algorithm where the problem is divided into a series of the traditional material-void phase topology optimization. The main contribution of their work is using different levels of discretization for the displacement, design variable and density mesh which results in optimal designs with higher resolutions.

1.2. Simultaneous material gradation and topology optimization of FGMs

In multi-material design, there is a sharp and abrupt transition between material phases; the designs are therefore vulnerable to interlaminar stresses and cracking [24]. Functionally graded materials (FGM) overcome this problem by allowing for a smooth and continuously varying material distribution. A typical application of FGM are metal-ceramic structures subject to severe thermal environment [25].

Optimization of FGMs can be performed by removing the restriction of a single phase at each point within the domain [24]. This will typically lead to optimal structures with better performance at the expense of using more advanced fabrication technologies. In this paper, we will use the terminologies "*multi-material topology optimization*" and "*functionally graded topology optimization*" to distinguish between the two types.

While there are numerous studies on multi-material topology optimization, research on topology optimization of FGM structures is less prevalent. Also, most of such studies are dedicated to the design of piezocomposites used in piezoelectric transducers and piezo-actuators [26–29]. In case of compliance minimization, as one of the earliest studies, Paulino and Silva [30] introduced a so-called FGM-SIMP topology optimization where the material properties are considered to vary according to some pre-determined profiles. Gradation of material properties is modelled by using the graded finite element method and the so-called continuous topology optimization problem is solved by using an optimality criteria. A few years later, Almeida et al. [31] introduced a global-local approach for the investigation of layout and material gradation in topology optimization of FGMs by employing the same concept. The proposed formulation is associated to symmetry and

pattern repetition constraints, including material gradation effects at both global and local levels [31]. Moreover, topology optimization of functionally graded cellular materials was recently investigated by Ramadan et al. [32] where microstructure of the FGM is assumed to be composed of a series of base cells in the variation direction and self-repeated in other directions. A bi-directional evolutionary structural optimization (BESO) technique in the form of inverse homogenization is subsequently used for the design of the FGM for specified variation in bulk or shear modulus [32].

In 2008, Xia and Wang [24] proposed a level set based method for simultaneous optimization of material properties and topology of FGM structures. The volume fractions of the constituent phases and the structural boundary are considered as the design variables, with the former being discretized as a scalar field and the latter being implicitly represented by the level set method [24]. The two design variables are integrated into a common objective functional and the decent directions are obtained via the sensitivity analysis. The optimization process is accordingly expressed as the solution to a coupled Hamilton–Jacobi equation and diffusion partial differential equation [24]. Recently, an evolutionary approach which is inspired by the heuristic nature of BESO and genetic algorithm (GA) is proposed to address the same optimization type [33].

1.3. Topology optimization by the isogeometric analysis method

The isogeometric analysis method, introduced by Hughes et al. [1] in 2005, with the primary advantages of exact modelling of the geometry, and removing the need for an independent mesh generation tool has recently attracted tremendous attention from researchers in the field of computational mechanics. Owing to the main merits of this method, namely, it eliminates the need for remeshing during the optimization process, and creates smooth surface boundaries, some of the earlier studies focused on applying of this method for structural shape optimization; see [34–41] and references therein. However, all of these studies were restricted to single material topology optimization.

In the earliest studies, the idea of trimming techniques of CAD surfaces [42–44] was introduced for creating arbitrary complex topologies from the CAD files created using NURBS which removes the additional post-processing and CAD recovery stages required for communication with CAD systems. In later studies, researchers employed the IGA method in phase field models

and density based approaches [45–49]. Dede et al. [45] considered a phase field model based on the generalized Cahn-Hilliard equation to address two and three-dimensional topology optimization problems for compliance minimization. Hassani et al. [47] derived and implemented an optimality criterion for the topology optimization of plane elasticity problems using the NURBS based isogeometric method. The composition of isogeometric analysis with a radial basis function (RBF) level-set method for topology optimization was investigated by Shojaee et al. [49]. A new IGA method was introduced by Tavakkoli and Hassani [46], where an implicit function is constructed over the design domain using NURBS parameterization while an optimality criterion is derived to improve the implicit function towards the boundaries.

Qian [48] presented a new form of density based topology optimization by using B-splines as the design space so that an arbitrarily shaped design domain is embedded into a rectangular domain in which tensor-product B-splines are used to represent the density field. The study shows that this representation provides an intrinsic filter for topology optimization whose size is controlled by B-spline degrees and resolution and is effective in removing numerical artifacts as well as controlling minimal length scales. Such representation decouples the design space of density distribution from the finite element mesh so that multi-resolution designs can be obtained where a variety of FE techniques can be used for the solution of equilibrium equations and different methods can be employed to project the B-spline density into the analysis space. The same concept has recently been applied to 3D problems [50] and is shown to dramatically reduce the required storage space of the usual density filters. Finally, the application of IGA for the analysis, shape and material properties optimization of composite and FGM structures have recently been studied in [25,41,51–53].

In the present study, we apply the isogeometric analysis method for simultaneous material distribution and topology optimization of structures comprised of multiple distinct or graded materials with the imposition of either volume fraction or mass constraint. Moreover, an extension of the perimeter control technique for multimaterial optimization will be introduced. The proposed method provides the possibility of direct controlling the minimal lengths scales of each material phase, as well as controlling the transition rate between material phases in case of functionally graded materials. As will be discussed later, unlike the common element or nodal based density representations in the classic FEM, the required density gradients for such

restrictions will be computed exactly with no additional cost owing to the higher order continuity of the utilized NURBS-based parameterization scheme. This in fact inspired us to extend and implement this restriction technique to an isogeometric multimaterial topology optimization method. For a comparative discussion on different existing restriction techniques refer to [6,54]. To the best of our knowledge, no such investigations within the framework of IGA have been reported in the literature thus far.

2. Problem formulation of isogeometric multi-material topology optimization

In this section, after a concise review multi-material elasticity equations, and their solution by the NURBS based IGA method, we present the formulation of a density based isogeometric topology optimization concept for the compliance minimization problem with multiple materials.

2.1. Governing multi-material elasticity equations

Let Ω be a 2D domain in $\mathbb{R}^2$ with the boundary $\partial\Omega = \partial\Omega_D \bigcup \partial\Omega_N$, where $\partial\Omega_D$ and $\partial\Omega_N = \partial\Omega \setminus \partial\Omega_D$ are the partitions of boundary where Dirichlet and Neumann boundary conditions are specified, respectively. The governing elasticity equations for a general linear elastostatics problem over Ω are

$$\begin{aligned} -div\,\tilde{\sigma}(\mathbf{u}) &= \mathbf{b} \quad && in\ \Omega, \\ \mathbf{u} &= \mathbf{u}_0 && on\ \partial\Omega_D, \\ \tilde{\sigma}(\mathbf{u}).\hat{\mathbf{n}} &= \bar{\mathbf{t}} && on\ \partial\Omega_N, \end{aligned} \tag{1}$$

where $\tilde{\sigma}$ is the stress tensor, $\mathbf{u}$ denotes the unknown displacement field, $\hat{\mathbf{n}}$ is the unit vector normal to the boundary $\partial\Omega$ and $\mathbf{b}$ is the body force vector. Also, $\mathbf{u}_0$ and $\bar{\mathbf{t}}$ are the prescribed displacement and traction boundary conditions. In the present case where the domain Ω is occupied by multiple material phases, the stress and strain fields are related by using the generalized Hooke's law as

$$\tilde{\sigma}(\mathbf{u}, \bar{\Theta}) = \mathbf{D}(\bar{\Theta})\varepsilon(\mathbf{u}) \tag{2}$$

where ε denotes the strain field and $\mathbf{D}$ is the fourth order effective elasticity tensor. Further, $\bar{\Theta} = \left[\Theta_0(\mathbf{x}), \Theta_1(\mathbf{x}), ..., \Theta_{\text{m-1}}(\mathbf{x})\right]$ is the vector of all density fields wherein $\Theta_k(\mathbf{x})$ represents the *k*th

material density distribution, and m is the number of candidate solid materials. As observed, the elasticity tensor is a function of the volume fractions of all material phases. We will discuss the evaluation of the effective elasticity tensor later. The relation between the displacement and strain fields is

$$\varepsilon(\mathbf{u}) = \frac{1}{2}(\nabla\mathbf{u} + \nabla\mathbf{u}^T) \tag{3}$$

We recall that in IGA, the geometry is usually constructed by a mapping from the parametric space (ξ, η) to the physical space (x, y) using an in-plane NURBS surface as

$$\mathbf{x}(\xi,\eta) = \sum_{i=0}^{n_1}\sum_{j=0}^{n_2} R_{i,j}^{p,q}(\xi,\eta)\mathbf{x}_{i,j} = \mathbf{RP}, \qquad \begin{matrix} 0 \le \xi \le 1 \\ 0 \le \eta \le 1 \end{matrix} \tag{4}$$

where $\mathbf{x} = (x, y)$ is the vector of physical coordinates, and $R_{i,j}^{p,q}(\xi,\eta)$ is the rational basis function of degree p and q in ξ and η directions, respectively, corresponding to $(i, j)th$ control point $\mathbf{x}_{i,j}$, defined as

$$R_{i,j}^{p,q}(\xi,\eta) = \frac{N_{i,p}(\xi)N_{j,q}(\eta)w_{i,j}}{\sum_{k=0}^{n_1}\sum_{l=0}^{n_2} N_{k,p}(\xi)N_{l,q}(\eta)w_{k,l}} \tag{5}$$

in which, $w_{i,j}$ are the associated weights to every control point and $N_{i,p}(\xi)$ and $N_{j,q}(\eta)$ are the normalized B-spline basis functions of degree p and q associated to the knot vectors $\boldsymbol{\Xi} = \{\xi_0, \xi_1, \ldots, \xi_{m_1}\}$ and $\mathbf{H} = \{\eta_0, \eta_1, \ldots, \eta_{m_2}\}$, respectively.

Following the extension of isoparametric concept, the unknown field variable(s) is also approximated using the same basis functions as

$$\mathbf{u}(\xi,\eta) \approx \sum_{i=0}^{n_1}\sum_{j=0}^{n_2} R_{i,j}^{p,q}(\xi,\eta)\mathbf{u}_{i,j} = \mathbf{Rd} \tag{6}$$

where $\mathbf{d}$ is the unknown vector of so-called control variables. Using the above approximation and following a standard variational approach, the equivalent algebraic form of the governing multi-material elasticity equations (1-3) could be obtained as

$$\mathbf{K}(\bar{\Theta})\mathbf{d} = \mathbf{f} \tag{7}$$

where **K** and **f** are the global stiffness matrix and force vector obtained via the assembly of patches if the geometry is modeled with multiple patches. Over a typical patch *e*, in the absence of body forces, these entities are derived as

$$\mathbf{K}^e(\bar{\Theta}) = \int_{\Omega_e} \mathbf{B}^T \mathbf{D}(\bar{\Theta})\mathbf{B} d\Omega, \tag{8}$$

$$\mathbf{f}^e = -\int_{\partial\Omega_N} \mathbf{R}^T \bar{\mathbf{t}} d\Gamma \tag{9}$$

where **B** is the matrix of derivatives of basis functions. It needs to be noted that, in order to formulate a continuous density based multi-material optimization problem, the elasticity tensor in (8) should be approximated in terms of the elasticity tensors of different contributing material phases. This is usually achieved by employing a so-called material interpolation scheme discussed below.

2.2. Material interpolation scheme

As mentioned in the previous sections, a variety of techniques have been suggested for the interpolation of material properties in case of multi-material topology optimization problem. The main considerations for such techniques are smooth convergence to the extreme values 0-1 for all the material phases so that ideally no overlap between the phases exists, physical realization, the ability of handling any number of material phases, as well as the applicability for constraints on both volume fractions and structural mass.

The initial idea was proposed by Sigmund and Torquato [15] as the extension of the SIMP method for three phase (two solid phases and void) topology optimization by using the following relation

$$\mathbf{D}(\bar{\Theta}) = \Theta_0^{\mu}(\mathbf{x})\left[(1-\Theta_1^{\gamma}(\mathbf{x}))\mathbf{D}_1 + \Theta_1^{\gamma}(\mathbf{x})\mathbf{D}_2\right] \tag{10}$$

where two density fields are introduced, one of which controls the existence of solid or void (Θ_0), while the other one (Θ_1) plays the role of selection between the two material phases. In above equation, μ and γ are the penalties assigned to these density fields to push the design

variables towards discrete 0-1 values. Further, $\mathbf{D}_1$ and $\mathbf{D}_2$ represent the elasticity tensors of solid materials 1 and 2. This scheme was later on extended by Stegmann and Lund [22] for *m* number of materials as follows

$$\mathbf{D}(\bar{\Theta}) = \Theta_0^{\mu}(\mathbf{x}) \sum_{i=1}^{m} W_i \mathbf{D}_i \tag{11}$$

where

$$W_i = \prod_{j=1}^{i-1} \left[1 - \Theta_{i, i \neq m}^{\gamma}(\mathbf{x}) \right] \Theta_j^{\gamma}(\mathbf{x}) \tag{12}$$

for which the following relation is always satisfied

$$\sum_{i=1}^{m} W_i = 1 \tag{13}$$

Equation (13) ensures the summation of solid material density fields to be equal to 1 at any point of the design domain and is critical for obtaining realistic optimal designs. This formulation has been proven to work efficiently for up to 3 material phases [22]. However, when the number of candidates are larger, the method tends to get stuck in local optima, and alternative schemes have been proposed [20,22]. It should be noted that, although the other interpolation schemes proposed as an alternative to equation (11), e.g. [20,22], are claimed to work better for a larger number of material candidates as well as in the presence of mass constraint [20], they fail to satisfy equation (13) and as a consequence are prone to give rise to unrealistic optimal designs. Therefore, in the present work, we limit our experiments up to 3 material phases and employ equations (10-13) for the material interpolation scheme with either the imposition of volume fraction or total mass constraint.

2.3. Formulation of the optimization problem

In order to define a meaningful topology optimization problem with multiple materials, different ideas exist. In the most common approach, the problem is defined as finding the optimal distribution of *m* candidate materials by the imposition of constraints on the volume fractions of $m-1$ material phases as well as on the overall volume fraction of the solid part. The

optimization problem for the special case of $m = 2$ (with two solid materials) could mathematically be expressed as follows

$$\begin{aligned} &\underset{\bar{\boldsymbol{\Theta}}}{\text{minimize}}\ J(\bar{\boldsymbol{\Theta}}, \mathbf{d}) = \mathbf{f}^T \mathbf{d} \\ &\text{subject to: } \mathbf{K}(\bar{\boldsymbol{\Theta}})\mathbf{d} = \mathbf{f} \\ &\qquad g_1(\boldsymbol{\Theta}_0) = \int_\Omega \Theta_0(\mathbf{x}) d\Omega - \bar{V}_0 \le 0, \\ &\qquad g_2(\bar{\boldsymbol{\Theta}}) = \int_\Omega \Theta_0(\mathbf{x})\left[1 - \Theta_1(\mathbf{x})\right] d\Omega - \bar{V}_1 \le 0 \end{aligned} \tag{14}$$

where J denotes the compliance, $\Theta_k(\mathbf{x})$ is the *k*th volume fraction (density) field with $\boldsymbol{\Theta}_k$ being its associated vector of design variables, and $\bar{\boldsymbol{\Theta}} = \left[\boldsymbol{\Theta}_0, \boldsymbol{\Theta}_1, ..., \boldsymbol{\Theta}_{\text{m-1}}\right]$ is a general vector including the design variables of all density fields. We will simply refer to $\bar{\boldsymbol{\Theta}}$ as the vector of design variables henceforth. Further, $\bar{V}_0$ and $\bar{V}_1$ represent the volume fraction constraints on the solid part and the first material, respectively. In optimization problem (14), the design variables must conform to the following prescribed geometric constraints

$$\mathbf{0} < \boldsymbol{\Theta}_{\min} \le \boldsymbol{\Theta}_0 \le \mathbf{1} \tag{15}$$

$$\mathbf{0} \le \boldsymbol{\Theta}_k \le \mathbf{1}, \quad (k = 1, ..., m-1) \tag{16}$$

where $\boldsymbol{\Theta}_{\min}$ is a small lower bound vector (e.g. $\Theta_{\min} = 10^{-9}$) used in order to avoid singularities.

As an alternative to formulation (14), we can set up a more practical optimization problem by the imposition of a constraint on the overall mass of the structure and allow for any fraction of material phases [20]. For this case, the statement of problem (14) changes to

$$\begin{aligned} &\underset{\bar{\boldsymbol{\Theta}}}{\text{minimize}}\ J(\bar{\boldsymbol{\Theta}}, \mathbf{d}) = \mathbf{f}^T \mathbf{d} \\ &\text{subject to: } \mathbf{K}(\bar{\boldsymbol{\Theta}})\mathbf{d} = \mathbf{f} \\ &\qquad g_1(\bar{\boldsymbol{\Theta}}) = \int_\Omega \Theta_0(\mathbf{x})\left[\rho_1(1 - \Theta_1(\mathbf{x})) + \rho_2 \Theta_1(\mathbf{x})\right] d\Omega - \bar{M} \le 0 \end{aligned} \tag{17}$$

where ρ_i denotes the real density of material phase *i* and $\bar{M}$ is the constraint on total mass of the structure. The design variables should similarly conform to (15), and (16). This formulation of the problem extends the design space by setting the optimization algorithm free to take any

fraction for each material phase, thereby resulting in better optimal designs. Moreover, the imposition of constraint on the overall structural mass is typically of interest in most engineering applications [55]. In this study, we will address both types of constraints. The optimization problems (14) and (17) could also be easily extended for any number of candidate materials by using equations (11) and (12). It is here necessary to clarify that, following the common terminology used in the literature, we may refer to $\Theta(\mathbf{x})$ as density field, while it always represents volume fraction distribution field. Henceforth, we drop $(\mathbf{x})$ for brevity and simply denote the *k*th density field by Θ_k .

As already mentioned, the performance of a proposed optimization method employed to address the above established density based optimization problems depends on the parameterization method of the density fields of material phases. We discuss below our proposed method.

2.4. NURBS-based representation of density fields

In the proposed isogeometric approach, we use a fully isogeometric NURBS based parameterization where the same basis functions employed for modelling the geometry and approximation of the solution are also used for the representation of density fields. That is,

$$\Theta_k(\xi,\eta)=\sum_{i=0}^{n_1}\sum_{j=0}^{n_2}R_{i,j}^{p,q}\left(\xi,\eta\right)\Theta_{i,j}^{k}=\mathbf{R}\boldsymbol{\Theta}_k\,,\quad (k=0,1,...,m-1) \tag{18}$$

From the geometric point of view, one can imagine equation (18) as the construction of different phases density fields by using NURBS surfaces over the computational domain where the applicates of their control points, i.e. $\Theta_{i,j}^{k}$, play the role of design variables. It will be seen that adopting such an idea will bring numerous advantages, discussed below briefly, compared to the common constant element-wise or nodal based density representation employed in the classic FEM topology optimization.

- *Checkerboard free design space.* Due to the tensor product nature of the NURBS based representation used for the description of density fields, it intrinsically acts as a filter and prevents checkerboard patterns. Compared to the usual distance based functions used for density filter in classic FEM, such filtering differs in terms of weight function as well as

the influence region. The shape of this filter is characterized by the existing physical mesh, where in particular, a $p \times q$ degree basis function acts as a filter with the effective length of $p+1$ knot elements in ξ and $q+1$ elements in η direction. Accordingly, the effective zone of this filter could be controlled by the order of basis functions and the resolution of discretization. It needs to be mentioned that the analytical studies performed in [48] for the filtering effect of B-spline space used in a multi-resolution FEM based topology optimization could be extended for the presented isogeometric NURBS based representation with slight modifications. Therefore, we do not discuss them here in further details and refer to this work [48].

- *Applicability of higher order basis functions.* Owing to the important convex hull property of NURBS surfaces, the above representation makes employing any desirable higher order of basis functions possible with the geometric constraints in (15) and (16) being satisfied by simply restricting the design variables to lie within the specified range. This is not the case when the concept of Continuous Approximation of Material Distribution (CAMD) is employed in other numerical methods such as FEM or meshless methods [56]. For instance, in FEM, researchers use bilinear shape functions for the interpolation of nodal densities even if higher order shape functions are employed for solution approximation to avoid exiting the density field from the interval [0,1]. This issue arises from the lack of non-negativity property of higher order Lagrange shape functions. Employing higher order basis functions provides higher order of continuity and differentiability. As will be seen later, this considerably simplifies the application of restriction methods to the topology optimization problem.
- *High resolution of the optimal results.* One of the most desired characteristics of a topology optimization framework is obtaining high resolution designs with a low computational cost for analysis and optimization. As will be observed in the presented numerical results, due to the smoothness of the employed basis functions used for continuous description of density fields, the obtained optimal designs are of quite high quality and smoothness on the boundaries even if the discretization is not very fine.
- *Efficient provision of analytical sensitivities.* Last but not least, as will be seen later, employing the same parameterization for both design and analysis space, will bring the

possibility of full analytical provision of sensitivities in a computationally efficient fashion.

2.5. Minimal length scale control

The continuous optimization problem as posed in (14) or (17) is ill-posed and does not admit the existence of the optimal solution [57]. This reveals as the mesh-dependency phenomenon during the numerical implementation so that refining the discretization will yield different optimal solutions with smaller length scales and lower compliance indefinitely. Hence, additional restrictions must be imposed in order to make the problem well-posed and achieve mesh-independency. Such restrictions could also be directly employed as a tool for controlling the minimal and sometimes maximal features length scale. So far, several studies have been performed and many different techniques have been proposed for this purpose the most common of which are local constraints on the density gradient [58], local density and sensitivity filters [58–60], global control of the minimum length scale [61], perimeter control or limitation [62–64], and projection techniques [65]. For a thorough review on these techniques and the discussion of their pros and cons refer to [6,66].

It is here necessary to mention that, although according to previous explanations, the employed NURBS space for density representation acts as an inherent filter, whose length could be controlled by *h* or *p*-refinement, and plays an effective role to remove checkerboard patterns, it has some shortcomings to be used for controlling minimal length scale. Mainly, due to employing the same parameterization for both the analysis and design space, it does not provide enough flexibility. One can come up with the idea of using multi-resolutions for the analysis and design space to resolve this issue and provide the possibility of using any higher order of basis functions for description of the density fields in the design space to control the filter size. However, such an idea will result in expanding the intermediate density zone in the optimum designs without the possibility of using a continuation method for diminishing it. Moreover, as will be seen later, it requires additional cost for the storage of density fields as well as the calculation of sensitivities.

In this study, inspired by the previously discussed advantages of the employed NURBS based representation of density fields such as higher order of continuity, we will make use of the

perimeter control technique where a global upper bound constraint in terms of the total variation of the density function is imposed on the optimization problem [54] as

$$g(\boldsymbol{\Theta}_0) \equiv \int_\Omega \left\| \nabla \Theta_0 \right\|_\beta d\Omega - \bar{P}_L \le 0, \quad \bar{P}_L > 0 \tag{19}$$

where $\|.\|_\beta$ denotes β-norm. For $\beta = 1$, g measures the perimeter of the density field. For $\beta = 2$, that will be used here, g measures the $L^2 - norm$ of the density field gradient which represents the total variation of the solid density field. The imposition of a perimeter constraint as (19) makes the topology optimization problem at hand well-posed, and enables us to directly control the complexity of the optimal designs as well as the minimal features lengths by the appropriate selection of parameter $\bar{P}_L$. It should be here noted that we will use the terminology "perimeter control" for a restriction method as (19), although it technically measures the total variation when $\beta = 2$ is used. As an alternative to equation (19), we can add a term of the following form to the objective function [54],

$$\alpha \int_\Omega \left\| \nabla \Theta_0 \right\|_\beta d\Omega, \quad \alpha > 0 \tag{20}$$

where α is the coefficient which plays the role of $\bar{P}_L$ in (19). The larger value of α will result in larger minimal lengths scales and simpler topologies, at the expense of extending the intermediate density regions. A continuation method could be simply used where the value of α is decreased after a certain number of iterations to avoid this issue, although the success of this strategy is not always guaranteed.

It sometimes might be of interest to also have control on the minimal lengths scales of some or all material phases for better manufacturability of the optimal designs. We extend here the above relations for such purpose in the presence of multiple material phases by the introduction of the following relations

$$g(\bar{\boldsymbol{\Theta}}) \equiv \sum_{i=0}^{m-1} \alpha_i \int_\Omega \left\| \nabla \Theta_i \right\|_\beta d\Omega - \bar{P}_L \le 0, \quad \bar{P}_L > 0 \tag{21}$$

$$\sum_{i=0}^{m-1} \alpha_i \int_\Omega \left\| \nabla \Theta_i \right\|_\beta d\Omega, \quad \alpha_i > 0 \quad \forall i = 0,1,..,m-1 \tag{22}$$

In above relations, α_i are weighting coefficients which should be properly adjusted for any problem to obtain desirable lengths scales for different material phases. Similarly, the first relation should be imposed as a global constraint while the latter should be embedded into the objective function. Although both of the above methods act the same with the common drawback of the inexistence of a straightforward way for the specification of suitable values of weighting coefficients to obtain the desired minimal lengths scales, based on our experiments, the latter approach is found to be more numerically stable. Hence, we will employ this method in our numerical tests. As will be observed in the numerical results, employing this idea will bring about optimal designs with desirable sizes for features composed of each of the materials which are considerably easier to fabricate. Moreover, mesh-independency could be achieved by appropriate selection of coefficients α_i.

Selection of suitable values for parameters α_i in (22) might be quite challenging and problem dependent since they should be specified with regards to the value of the objective function and dimensions of the geometry. In order to circumvent this issue and limit the choices for these variables, we present the following dimensionless form of the objective function

$$\underset{\boldsymbol{\Theta}_k}{\text{minimize}}\ \bar{J}(\bar{\boldsymbol{\Theta}},\mathbf{d},\bar{\boldsymbol{\alpha}}) = \mathbf{f}^T\mathbf{d}\Big/J_0 + \frac{1}{L_0}\sum_{i=0}^{m-1}\bar{\alpha}_i\int_\Omega \left\|\nabla\Theta_i\right\|_2 d\Omega, \quad (k=0,1,...,m-1) \tag{23}$$

where $\bar{J}$ is the dimensionless augmented objective function, $\bar{\boldsymbol{\alpha}}$ is the vector of perimeter coefficients i.e. $\boldsymbol{\alpha}=[\alpha_0,\alpha_1,...,\alpha_{m-1}]$, J_0 is the compliance of the initial design when made of the softest phase, and L_0 is a characteristic length of the structure. We use here the circumference of the initial design as the characteristic length. In the above non-dimensional augmented form of the objective function, $\bar{\alpha}_i$ are dimensionless coefficients which are now limited to a range of about $[0,1]$. Assigning $\bar{\alpha}_i$ as 0 implies no perimeter control, while assigning 1 will literally result in almost no topological changes. Practical values of $\bar{\alpha}_i$ should usually be selected from the range $[0,0.1]$ with regards to the volume fraction constraints of different phases and the desired level of complexity of their distribution.

In order to evaluate the integral expressions in (19)-(23), the gradients of density fields are required. As already pointed out, owing to the continuity of the employed NURBS based representation for the density fields, these gradients could be provided straightforwardly using the following relation

$$\nabla\Theta_k = \mathbf{R}_{,\mathbf{x}}\boldsymbol{\Theta}_k \tag{24}$$

where $\mathbf{R}_{,\mathbf{x}}$ is the matrix of derivatives of basis functions with respect to physical coordinates defined as

$$\mathbf{R}_{,\mathbf{x}} = \begin{bmatrix} \dfrac{\partial \mathbf{R}}{\partial x} & \dfrac{\partial \mathbf{R}}{\partial y} \end{bmatrix}^T \tag{25}$$

It is interesting to note that equation (24) yields the exact gradient of density fields at almost no cost, as the required derivatives of basis functions are already available from the computational model. It is here necessary to point out that due to lack of enough continuity, the evaluation of density fields gradients when the element or nodal based classic FEM is used is not this easily possible, no matter what order of shape functions is employed. The order of continuity in Lagrangian elements is always C^0 irrespective of the degree of shape functions, although higher order shape functions cannot even be easily used due to lack of the non-negativity property discussed above. As a result, more complex theories must be used to provide an estimation of the gradient of such non-differentiable density field [64].

Having the gradient of a density field from (24), its 2-*norm* required in (23) could be simply found using the following relation

$$\left\|\nabla\Theta_k\right\|_2 = (\nabla\Theta_k{}^T \nabla\Theta_k)^{1/2} \tag{26}$$

The above equation could be numerically integrated over the domain using the same Gauss quadrature rule employed for the calculation of stiffness matrix to evaluate the integral expression in (23).

2.6. Sensitivity analysis

In order to solve the established continuous optimization problems (14) or (17) by using a gradient based algorithm, the provision of sensitivities for the objective function and all the constraints is necessary. Due to the employed unified parametric representation for both analysis and design space, these sensitivities could be derived full analytically and in a straight forward manner as follows.

2.6.1. Sensitivity of the objective function

The sensitivity of the dimensionless objective function $\bar{J}$ in (23) could be written as follows

$$\frac{\partial \bar{J}}{\partial \Theta_{i,j}^{k}} = \frac{1}{J_0}\frac{\partial J}{\partial \Theta_{i,j}^{k}} + \frac{1}{L_0}\sum_{i=0}^{m-1}\bar{\alpha}_i \int_{\Omega}\frac{\partial \left\|\nabla \Theta_i\right\|_2}{\partial \Theta_{i,j}^{k}} d\Omega \tag{27}$$

In order to compute the sensitivity of the compliance J with respect to design variables $\Theta_{i,j}^{k}$, the adjoint method is used. Using equations (7) and (14) we can write

$$\frac{\partial J}{\partial \Theta_{i,j}^{k}} = \boldsymbol{\lambda}^{T}\frac{\partial \mathbf{K}(\bar{\boldsymbol{\Theta}})}{\partial \Theta_{i,j}^{k}}\mathbf{d} \tag{28}$$

where $\boldsymbol{\lambda}$ is the adjoint vector obtained via solving the adjoint equation $\mathbf{K}(\bar{\boldsymbol{\Theta}})\boldsymbol{\lambda} = -\mathbf{f}$. According to (28), in order to evaluate the sensitivity of the compliance, we need to have the derivatives of the stiffness matrix with respect to design variables $\Theta_{i,j}^{k}$. Using equation (8), we can derive the sensitivities of the stiffness matrix as

$$\frac{\partial \mathbf{K}^{e}}{\partial \Theta_{i,j}^{k}} = \int_{\Omega_e}\mathbf{B}^{T}\frac{\partial \mathbf{D}(\bar{\boldsymbol{\Theta}})}{\partial \Theta_{i,j}^{k}}\mathbf{B}d\Omega \tag{29}$$

which requires the derivatives of the elasticity tensor $\mathbf{D}(\bar{\boldsymbol{\Theta}})$. These derivatives could be provided by using the chain rule as

$$\frac{\partial \mathbf{D}(\bar{\boldsymbol{\Theta}})}{\partial \Theta_{i,j}^{k}} = \frac{\partial \mathbf{D}(\bar{\boldsymbol{\Theta}})}{\partial \Theta_{k}}\frac{\partial \Theta_{k}}{\partial \Theta_{i,j}^{k}} \tag{30}$$

By employing equations (11), (12) and (18), the required partial derivatives in the above relation are obtained as (31) and (32).

$$\frac{\partial \mathbf{D}(\bar{\boldsymbol{\Theta}})}{\partial \Theta_k} = \begin{cases} \mu \Theta_0^{\mu-1} \sum_{i=1}^{m} W_i \, \mathbf{D}_i & \text{if } k = 0 \\ \Theta_0^{\mu} \left[\prod_{j=1}^{k-1} (-\gamma \Theta_{k,k\neq m}^{\gamma-1}) \Theta_j^{\gamma} \right] \mathbf{D}_k & \text{otherwise} \end{cases} \qquad (k = 0,1,...,m-1) \tag{31}$$

$$\frac{\partial \Theta_k}{\partial \Theta_{i,j}^k} = R_{i,j}^{p,q}(\xi, \eta) \tag{32}$$

For the special case of $m=2$, equations (30-32) give

$$\frac{\partial \mathbf{D}(\boldsymbol{\Theta}_0, \boldsymbol{\Theta}_1)}{\partial \Theta_{i,j}^k} = \begin{cases} \mu \Theta_0^{\mu-1} \left[(1-\Theta_1^{\gamma}) \mathbf{D}_1 + \Theta_1^{\gamma} \mathbf{D}_2 \right] R_{i,j}^{p,q}(\xi, \eta), & k = 0 \\ \Theta_0^{\mu} \left[(-\gamma \Theta_1^{\gamma-1}) \mathbf{D}_1 + \gamma \Theta_1^{\gamma-1} \mathbf{D}_2 \right] R_{i,j}^{p,q}(\xi, \eta), & k = 1 \end{cases} \tag{33}$$

Considering equation (32), we can notice that the sensitivity of a density field with respect to its design variables is the same as basis functions which are already computed for the analysis. Since these functions do not change during the optimization process, they could be pre-stored when evaluated for the analysis without using additional storage space. This makes the sensitivity analysis cost effective.

Finally, the sensitivity of the *2-norm* of *k*th density field gradient could be obtained as

$$\frac{\partial (\left\| \nabla \Theta_k \right\|_2)}{\partial \Theta_{i,j}^k} = \frac{\nabla \Theta_k{}^T \mathbf{R}_{,\mathbf{x}}}{\left\| \nabla \Theta_k \right\|_2} \tag{34}$$

Equation (34) shows that, in order to calculate the sensitivities of the perimeter control term, the derivatives of basis functions are necessary. Again, one can see that these derivatives are already available from the computational model and do not pose any additional cost.

2.6.2. Sensitivity of the optimization constraints

We here derive the sensitivities for both the volume fraction and mass constraints. The sensitivities of the volume fraction constraints in (14) could be simply obtained as

$$\frac{\partial g_1(\boldsymbol{\Theta}_0)}{\partial \Theta_{i,j}^k} = \begin{cases} \int_\Omega R_{i,j}^{p,q}(\xi,\eta)\, d\Omega, & k=0 \\ 0, & k=1 \end{cases} \tag{35}$$

$$\frac{\partial g_2(\boldsymbol{\Theta}_0,\boldsymbol{\Theta}_1)}{\partial \Theta_{i,j}^k} = \begin{cases} \int_\Omega R_{i,j}^{p,q}(\xi,\eta)(1-\Theta_1) d\Omega, & k=0 \\ -\int_\Omega R_{i,j}^{p,q}(\xi,\eta)\Theta_0 d\Omega, & k=1 \end{cases} \tag{36}$$

The important point about the above equations is that, according to (35), the sensitivities of g_1 are invariable with respect to the optimization iterations and could be pre-stored, while the sensitivities of g_2 need to be performed iteratively. Similarly, the sensitivities of the mass constraint in (17) could be derived as

$$\frac{\partial g_1(\boldsymbol{\Theta}_0,\boldsymbol{\Theta}_1)}{\partial \Theta_{i,j}^k} = \begin{cases} \int_\Omega R_{i,j}^{p,q}(\xi,\eta)\left[\rho_1 + \Theta_1(\rho_2-\rho_1)\right] d\Omega, & k=0 \\ (\rho_2-\rho_1)\int_\Omega R_{i,j}^{p,q}(\xi,\eta)\Theta_0 d\Omega, & k=1 \end{cases} \tag{37}$$

As observed, equation (37) is variable with respect to the optimization iterations and should be evaluated repeatedly.

2.7. Simultaneous isogeometric material gradation and topology optimization of FGMs

The presented multi-material optimization method could be easily altered for functionally graded structures by modifying the employed material interpolation scheme so that the estimated effective properties of the structure are physically realizable by FGMs. Several techniques have been suggested for the approximation of the effective material properties of an FG structure by having the volume fractions of the constituent phases at an arbitrary point. These strategies are classified into two main categories of mixture rules which only rely on the volume fractions of constituent materials, and micromechanics techniques which also consider the dimensions and geometry of periodic materials [24]. One of the popular mixture rules that is often employed by researchers is the Hashin-Shtrikman bounds [67]. In case of 2D, for two phase isotropic composite materials with the equal Poisson's ratio of $1/3$, the theory reduces to the following conditions on Young's modulus [67]

$$E(\Theta_1)^{-}_{HS} = \frac{(2+\Theta_1)E_1 + (1-\Theta_1)E_2}{2(1-\Theta_1)E_1 + (1+2\Theta_1)E_2} E_2 \tag{38}$$

$$E(\Theta_1)^{+}_{HS} = \frac{\Theta_1 E_1 + (3-\Theta_1)E_2}{(3-2\Theta_1)E_1 + 2\Theta_1 E_2} E_1 \tag{39}$$

where E_1 is the Young's modulus of harder material. Although micromechanics techniques yield more realistic estimation of the effective properties of FGMs, similar to the other existing studies in the literature [24,33], we employ here the average of the lower and upper Hashin-Shtrikman bounds in (38) and (39) as our material model to provide the possibility of a fair comparison with their results, that is

$$E(\Theta_1) = \frac{1}{2}\left(E(\Theta_1)^{-}_{HS} + E(\Theta_1)^{+}_{HS} \right) \tag{40}$$

Modification of equation (10) based on the above material model, yields

$$\mathbf{D}(\boldsymbol{\Theta}_0, \boldsymbol{\Theta}_1) = \Theta_0^{\mu}(\mathbf{x}) \left[\frac{1}{2}\left(\mathbf{D}(\Theta_1)^{-}_{HS} + \mathbf{D}(\Theta_1)^{+}_{HS} \right) \right] \tag{41}$$

where $\mathbf{D}(\Theta_1)^{-}_{HS}$ and $\mathbf{D}(\Theta_1)^{+}_{HS}$ are the lower and upper bounds on the elasticity matrix of the graded zone which are obtained using relations (38) and (39), respectively.

3. Numerical experiments

In this section, we present several numerical examples in order to demonstrate the performance and efficacy of the proposed isogeometrical methodology. To this purpose, a computer program in FORTRAN language is developed based on the presented formulation for the compliance minimization of 2D elasticity problems. Numerical studies are performed for the structures composed of two or three material phases with the imposition of either volume fraction or overall mass constraint. The performance of the obtained optimal results are compared to the corresponding single material designs as well as the available results in the literature. In order to solve the optimization problems, we employ the Method of Moving Asymptotes (MMA) [68],

which is well-known as one of the most powerful gradient-based algorithms suitable for topology optimization. We make the following assumptions for all the numerical experiments unless stated otherwise in a particular example. The problems are assumed to be under the plane stress state with unit thickness. A continuation method is adopted for the penalties μ and γ, starting from 1 with an increment of 0.02 per iteration until they reach 3, to reduce the possibility of convergence to local optima. It should be noted that in some cases, in order to avoid intermediate densities, larger values of penalties are required. When this has been the case, after the termination of optimization process, an additional analysis step with setting the penalties back to 3 has been performed and the compliance has been reevaluated to provide making a fair comparison with the other cases. Similarly, a continuation method is employed for perimeter control coefficients $\overline{\alpha}_i$ so that after certain number of iterations they are gradually diminished to small values during the optimization procedure to avoid grey-scale regions. The optimization process is terminated when the maximum change of design variables is lower than 0.05 in two consecutive iterations or the number of iterations reaches 1000. In all the examples, we start the optimization process from initially feasible designs with uniform and identical distribution of material phases. The problems are modelled by using quadratic basis functions in both directions. We use the Conjugate Gradient (CG) method with incomplete LU preconditioner for the solution of system of equations. Finally, the experiments are performed on a desktop computer with quad Core i7 CPU of 3.6 GHz clock speed and 16 GB of RAM.

3.1. Test case 1- L-bracket

In the first example, we consider the compliance minimization of an L-bracket with mass constraint, which is already studied by Gao and Zhang [20]. The configuration of the bracket is shown in Figure 1. A point load of magnitude $F = 100\,kN$ is applied in the vertical direction to the middle of the front edge. We employ a mesh of 64×128 knot elements for modeling the geometry. The problem is modelled using a single patch by repeating the control points located on the middle corners of the bracket. The structure is assumed to be comprised of two materials with the properties listed in Table 1.

Table 1. Material properties of *M1* and *M2*.

Material	E (*GPa*)	$\rho(kg/m^3)$	E/ρ
$M1$	105	5400	0.194
$M2$	70	2700	0.259

As the first case, we impose a constraint of $\bar{M} = 30\times10^3\, kg$ on the overall mass of the structure and study the effect of employing multiple materials on the performance of the optimal design compared to the single material ones. The problem is run for both single material cases as well as the multi-material one and the obtained optimization results are presented in Table 2.

Table 2. Optimization results for the L-bracket with $\bar{M} = 30\times10^3$.

Material	$\bar{\alpha}_0(\times10^{-3})$	Compliance	iterations	Time (*min*)
$M1$	6.0	23.02	277	6.5
$M2$	2.5	19.53	354	7.3
$M1\&M2$	3.5	18.77	346	10.0

It should be noted that the presented values for the perimeter coefficient $\bar{\alpha}_0$ in Table 2 have been selected with regards to the desired complexity of the optimal designs after performing a few trials. Also, no perimeter constraint on the material phases is imposed in the multi-material case, that is $\bar{\alpha}_1 = 0$. The presented optimization results in Table 2 are also in good agreement with the results of Gao and Zhang [20], which are 10.77, 9.57 and 9.02 for the minimization of strain energy with $M1$, $M2$ and $M1\&M2$, respectively. It needs to be noted that the slightly lower values of the objective functions reported in [20], result from using different material interpolation schemes as well as filtering values. In particular, they use an interpolation scheme which violates relation (13), and as already discussed, does not lead to realistic optimum results.

According to Table 2, the optimal result in case of multi-material design yields the best performance and has the highest computational cost. The higher computational cost mainly results from the sensitivity analysis with respect to the larger number of design variables which is twice that of the single material cases. The corresponding optimal results for each of the

studied cases are depicted in Figures 2(a)-(c). The multi-material optimum design shown in Figure 2(c) is comprised of 10.0% of $M1$ in volume, which implies the dominance of the contribution of $M2$ in this design. The distribution of different phases in the optimal design could be interpreted by observing the material properties of the constituent phases in Table 1. According to this table, $M1$ has a higher stiffness but a lower stiffness to mass ratio compared to $M2$. As the figure shows, the optimum structure is composed of $M1$ in regions which are prone to higher stress values in order to exploit its higher stiffness for the minimization of the compliance. However, in other parts of the structure the optimization algorithm favors $M2$ with the lower density and higher stiffness to mass ratio.

In general, the contribution of different phases in the presence of overall mass constraint highly depends on the value of mass constraint. In order to clarify this, we conduct the optimization problem with the imposition of different mass constraints and investigate the contribution of material phases in the optimum designs. The obtained results for the volume fractions of $M1$ and $M2$ in the optimum designs with different mass constraints are represented in Figure 3. As the figure shows, by increasing mass constraint the contribution of the stiffer phase, i.e. $M1$, increases. It could be observed that for the values of mass constraint lower than around $60\times10^3 kg$ the contribution of $M2$ is dominant, while for less restrictive mass constraints the contribution of $M1$ with higher stiffness prevails. The distribution of material phases in the optimal structures are depicted in Figure 4 for some typical values of mass constraint. The figure shows how the distribution of $M1$ expands within the optimum structures by increasing mass constraint.

In order to better reveal how employing multiple materials effects the performance of the optimal designs subjected to different mass constraints, we also perform the optimization problem using single materials $M1$ and $M2$, and compare the performance of the obtained results to multi-material designs. Figure 5 illustrates the compliances of multi-material designs for different mass constraints which are normalized by the respective compliances of single material designs with $M1$ and $M2$.

According to this figure, as it was expected, the illustrated compliance ratio is always lower than 1 implying the better performance of multimaterial designs for all mass constraints. Moreover,

the figure demonstrates that by decreasing mass constraint, the performance of multi-material design substantially increases compared to the single material design with $M1$, while it follows the opposite trend compared to single material designs with $M2$. It can be observed that the most increase in the performance of multi-material designs compared to the single material ones with $M1$ occurs at the lowest studied mass constraint, that is $\bar{M} = 15 \times 10^3 kg$, while it happens at $\bar{M} = 43.2 \times 10^3 kg$, which is the total mass of the full L-bracket made of $M2$, in comparison with the single material design with $M2$. According to the figure, the two curves intersect at a mass constraint of about $\bar{M} = 41.5 \times 10^3 kg$ which is highlighted in the figure. This is in fact a critical point indicating the mass constraint for which both single material designs yield the same performance and the multi-material design yields the highest performance with roughly 15% reduction of the compliance compared to both single material designs. Hence, the vicinity of this point is regarded as a desirable zone where using multi-material design will result in considerable higher performance. As can be seen, for any lower mass constraints, a single material design with $M2$ will have a better performance than that of $M1$, while for larger mass constraints it is the other way round.

3.2. Test case 2- MBB beam

As the second example, we consider the optimization of an MBB beam composed of three material phases subjected to volume fraction constraints on the constituent phases. The geometry and boundary conditions of the beam are illustrated in Figure 6. A downward unit load $F = 1$ is applied to middle top of the beam. The beam is assumed to be composed of three materials with stiffness ratios of $E1 : E2 : E3$ as 4:2:1, and the volume fraction constraints of 0.15:0.15:0.2. Due to symmetry, only half of the structure is modelled for the analysis and optimization to reduce the computational cost. A mesh of 122×60 knot elements is used for the modelling of the problem.

In this example, we investigate the ability of the proposed method in controlling the minimal lengths scales of different material phases by manipulating parameters $\bar{\alpha}_i$ in (23). We perform the optimization problem for four different sets of choices for parameters $\bar{\alpha}_i$ as listed in Table 3.

Table 3. Perimeter control coefficients $\bar{\alpha}_i(\times 10^{-3})$ for the optimization of the MBB beam.

Case No.	$\bar{\alpha}_0$	$\bar{\alpha}_1$	$\bar{\alpha}_2$
1	9.00	0.00	0.00
2	9.00	0.45	0.45
3	9.00	0.90	0.90
4	6.75	4.50	4.50

The obtained optimal designs for the studied cases including the distribution of different material phases are represented in Figure 7. As the figure shows, the same complexity for the optimum topologies has been obtained in all four cases with the selected parameters for $\bar{\alpha}_i$ listed in Table 3. Nevertheless, the distribution of material phases within the optimum designs are different. According to Figure 7(a), without the imposition of any constraints on material phases, the optimum design contains tiny features of all material phases throughout the structure with a large interface between them. It is evident that such design is hard to fabricate and is also quite susceptible to interlaminar stresses and cracking. Comparison of Figures 7(a)-(d) reveals that by increasing parameters $\bar{\alpha}_1$ and $\bar{\alpha}_2$, the optimum structures contain larger lengths scales of any of the material phases with less interface boundaries between them so that in case 4 each member of the truss-like optimum design is only composed of a single material. This substantially improves the manufacturability of the optimum designs and reduces the possibility of structural failure.

For a more detailed comparison, the optimization results including the compliance of the optimum designs as well as the perimeter of different density fields are presented in Table 4.

Table 4. Final density fields perimeters and optimization results for the MBB beam.

Case No.	P_L^0	P_L^1	P_L^2	Compliance	Iterations	Time (*min*)
1	147.12	231.87	328.52	16.88	793	20.1
2	169.69	74.91	37.15	16.66	941	30.4
3	170.72	68.78	37.73	16.68	916	26.1
4	181.86	61.03	24.69	16.74	882	22.7

In this table, P_L^k denotes the L^2-norm of kth material density field gradient in the optimal designs defined as

$$P_L^k = \int_\Omega \left\| \nabla \Theta_0 \right\|_2 d\Omega \tag{42}$$

Having examined the table, we can observe that by increasing $\bar{\alpha}_1$ and $\bar{\alpha}_2$, the perimeter of the entire solid density field, i.e. P_L^0, gently increases, while the perimeters of material phases decrease. Lower perimeter of materials density fields corresponds to less interface between different materials and larger lengths scales of them. It is interesting to note that the compliance of the optimum designs for cases with material perimeter control just slightly change by decreasing the material perimeters. This implies that using the proposed perimeter control technique, we can achieve much more manufacturable designs with slightly lower performance. Considering the table, we can see that in case 1 with no perimeter control a higher compliance is obtained, while it was expected the opposite. This could be attributed to the fact that in this case, the interface between material phases is many times larger than the cases with perimeter control. Since in the transition zone between material phases the intermediate densities are penalized, the compliance artificially increases. However, this artificial effect is negligible in cases with material perimeter control due to the relatively small difference between the material perimeters. The table also shows that the number of optimization iterations are approximately twice the previous example of the optimization of L-bracket with two material phases.

3.3. Test case 3- Quarter annulus

In order to demonstrate the ability of the proposed isogeometrical method in exact modelling of more complex geometries, in this example, we address the multi-material optimization problem of a quarter annulus studied by Dede et al. [45] for single material case by using a phase field model. The configuration of the annulus is depicted in Figure 8. The ring is assumed to be under the plane strain state and clamped at the bottom. A distributed load $\bar{t} = 200\,MPa$ is applied to the top left corner of the ring over a length of $S = \pi/10\,m$. We assume the annulus to be composed of Steel and Aluminum with the properties listed in Table 5. A mesh of 140×58 knot elements is used for modelling of the annulus.

Table 5. Material properties of Steel and Aluminum.

Material	E (GPa)	$\rho(kg/m^3)$	E/ρ
Steel	200	7800	0.0256
Al	70	2707	0.0258

For the sake of verification, we first address the single material optimization of the Steel annulus with the imposition of a volume fraction constraint $\bar{V}_0 = 0.35$ and compare the obtained results with those of [45]. The optimization results along with the selected perimeter control coefficient are presented in Table 6 and the obtained optimal topology is represented in Figure 9. As can be observed, the exact representation of the boundaries of the annulus is maintained in the optimal design. The compliance of this design is 89.61% lower than the compliance of the initial full bracket with $\Theta_0 = 0.35$. This is also in good agreement with the result reported by Dede et al. [45], where 88.47% reduction of the compliance is achieved at the steady state when a two-level continuation procedure is employed in a phase field model. The mass of the optimum structure is 6432.4 *kg*.

Table 6. Optimization results for the single material design of Steel annulus.

Mesh resolution	$\bar{\alpha}_0(\times 10^{-3})$	Compliance	Iterations	Time (min)
140×58	18.8	1.394	334	6.3

Next, we deal with multi-material optimization of the annulus by adding an additional *Al* phase to the design space and the imposition of a mass constraint the same as the optimal annulus mass in the previous case, that is $\bar{M} = 6432.4\,kg$. However, performing the optimization problem with this mass constraint will result in an optimal structure fully made of *Al*. Hence, we apply an additional constraint to the optimization problem so that the mass of *Al* is restricted to the maximum of 20% of the total mass of the optimal design. Furthermore, in order to investigate the mesh-independency of the proposed method, we conduct the optimization problem by using three different meshes for the annulus. The number of elements and selected perimeter control parameters for each case are presented in Table 7 along with the corresponding optimization

results. As the table shows, the same values of perimeter coefficients are selected for all the studied meshes.

Table 7. Perimeter control coefficients and optimization results for multi-material design of the annulus.

Mesh resolution	$\bar{\alpha}_0(\times 10^{-3})$	$\bar{\alpha}_1(\times 10^{-3})$	Compliance	Iterations	Time (*min*)
98×40	20.0	3.0	1.339	353	3.1
140×58	20.0	3.0	1.328	634	14.3
175×73	20.0	3.0	1.326	1000	32.5

The optimal topologies including the distribution of different materials are depicted in Figures 10(a)-(c) for different studied meshes. Considering these figures, we can see that the same topologies with similar distribution of material phases within the optimal designs have been achieved for the first two meshes, while the obtained topology in the third case is slightly different. This could be justified with regards to the existence of multiple local optima near the global optimum in topology optimization problems besides the sensitivity of parameters $\bar{\alpha}_i$ to the local optima. According to Table 7, the obtained compliances for the second and third meshes are only 0.15% different which further supports the provided argument. In general, slight tunings of the perimeter control coefficients might be needed in some cases to ensure convergence to the same local optimum and achieve perfect mesh-independency which could be regarded as a drawback of this technique.

As Table 7 indicates, by refining the mesh, lower values of compliance are achieved after a larger number of optimization iterations. As observed, in case of finest mesh resolution, the maximum allowed number of iterations has been achieved. If more number of iterations are allowed, the optimization process will terminate after 65 more iterations with negligible discrepancy in the optimal design.

Comparison of the compliance of the optimal multi-material design for the 140×58 mesh, with that of the optimal Steel annulus design using the same mesh resolution indicates 4.75% decrease of the compliance in case of multi-material design. It is interesting to note that this reduction of

compliance is accomplished, while the overall mass of the optimum designs are the same and, according to Table 5, the stiffness to mass ratio of both material phases are very close.

3.4. Test case 4- FGM Bridge

As the final numerical experiment, we investigate the applicability of the introduced method for simultaneous optimization of material gradation and topology of an FGM bridge-type structure which has already been studied by Xia and Wang [24], and Jebeli and Panahi [33]. The geometry and boundary conditions of the bridge are demonstrated in Figure 11. A downward unit load $F=1$ is applied to the bottom center of the bridge. The bridge is assumed to be composed of two materials with the Young's modules of $E_1=1$ and $E_2=0.25$. Volume fraction constraints are imposed to the solid and the stiffest phase (E_1) density fields as $\bar{V}_0=0.3$ and $\bar{V}_1=0.1$. The lower and upper bound geometric constraints corresponding to the design variables of the stiffest phase density field are specified as $\mathbf{0.1} \le \boldsymbol{\Theta}_1 \le \mathbf{0.9}$. Due to symmetry, only half of the bridge is modelled to reduce the computational effort. We conduct the optimization problem for four different choices of perimeter control parameters and compare the obtained optimal results against each other as well as the existing results in the literature. The selected optimization parameters together with the respective optimization results are presented in Table 8.

Table 8. Perimeter control coefficients and optimization results for the topology design of the FGM bridge.

Case No.	$\bar{\alpha}_0(\times 10^{-3})$	$\bar{\alpha}_1(\times 10^{-3})$	Compliance	Iterations	Time (*min*)
1	0.90	0.35	41.01	438	8.9
2	0.90	0.70	41.37	376	7.8
3	0.90	1.50	41.69	548	12.6
4	1.10	1.85	42.10	753	18.5

The corresponding optimal designs including the distribution of the strong phase (E_1) are indicated in Figure 12. The illustrated optimum designs in this figure are also in keeping with the available results in the literature [24,33]. As the figure shows, by increasing $\bar{\alpha}_1$, optimal designs with larger lengths scales of the stiffer phase, and smoother transition between material phases

are achieved. In addition, as $\bar{\alpha}_1$ increases, the two inner members of the bridge become closer to each other and are comprised of a smaller portion of the stiffer phase. Similar to the observation in previous examples, according to Table 8, these designs yield only slightly different performances compared to each other. The table shows that the least compliance occurs in case 1 with the lowest value for $\bar{\alpha}_1$. This optimal design has also a much better performance, i.e. 15.85% lower compliance, compared to the result of Xia and Wang [24] that is 48.735, suggesting the superiority of the proposed method.

It should be noted that, in this example, no continuation method has been used so that the perimeter control coefficients are constant throughout the optimization process. Consequently, using larger values of $\bar{\alpha}_1$, results in larger transition zone, and ensures a smoother transition between material phases which is quite desirable when FGMs are employed. If the gradation of material constituents happens in an abrupt manner, it reduces the manufacturability of the optimum FGM designs [69,70]. As observed, the employed perimeter control technique also provides the possibility of controlling the rate of transition between different material phases which meets manufacturing considerations.

4. Conclusion

A density based multi-material topology optimization method within the framework of isogeometric analysis approach was introduced. In this method, the density fields of different material phases are represented by using the same NURBS-based parameterization employed for both the geometry and analysis space. As observed, employing such unified parameterization brings many advantages compared to the element-wise or nodal based density representations commonly used in the classic FEM such as having desired level of continuity, full analytical provision of sensitivities in a cost effective manner, checkerboard free design space, and obtaining optimal designs with high quality. An extension of the perimeter control restriction technique was introduced and successfully implemented into the proposed isogeometrical method where weighted expressions in terms of L^2-norms of the gradient of different density fields were embedded to the objective function. By virtue of the employed density

representation, the required gradients of density fields were provided exactly in an efficient fashion. As verified by the numerical examples, this technique brings the possibility of direct control of minimal lengths scales of material phases as well as the complexity of the optimum designs. It was seen that this idea results in optimum designs with desirable lengths scales of different materials which dramatically enhances the manufacturability of the optimum designs with negligible change in their performance.

The method was successfully applied to the optimization problems with two or three material phases formulated for both volume fraction and total mass constraints. Numerical studies demonstrated superior performance of multi-material designs compared to the corresponding single material ones, and the consistency of the obtained results with the existing results of other numerical methods in the literature. The study revealed that in the presence of total mass constraint, the contribution of material phases in the optimum design depends on the magnitude of the applied mass constraint so that for less restrictive mass constraints, the contribution of the stiffer phase(s) increases.

In particular, the method was applied to topology design of functionally graded materials where the perimeter control technique could effectively be employed for controlling minimal lengths scales of material constituents as well as the gradation rate of the transition between the constituent phases. Moreover, superior performance of the proposed method compared to the available studies in the literature, besides yielding more manufacturable designs, was demonstrated. Overall, the suggested isogeometrical approach provides a powerful and robust tool for the topology design of structures with multiple materials which takes account of manufacturing considerations.

References

[1] Hughes TJR, Cottrell JA, Bazilevs Y. Isogeometric analysis: CAD, finite elements, NURBS, exact geometry and mesh refinement. *Comput Methods Appl Mech Eng* 2005; **194**:4135–95. doi:10.1016/j.cma.2004.10.008.

[2] Wang Y, Luo Z, Kang Z, Zhang N. A multi-material level set-based topology and shape optimization method. *Comput Methods Appl Mech Eng* 2015; **283**:1570–86. doi:10.1016/j.cma.2014.11.002.

[3] Wang MY, Wang X. "Color" level sets: a multi-phase method for structural topology optimization with multiple materials. *Comput Methods Appl Mech Eng* 2004; **193**:469–96. doi:10.1016/j.cma.2003.10.008.

[4] Wang MY, Wang X. A level-set based variational method for design and optimization of heterogeneous objects. *CAD Comput Aided Des* 2005; **37**:321–37. doi:10.1016/j.cad.2004.03.007.

[5] Van Dijk NP, Maute K, Langelaar M, Van Keulen F. Level-set methods for structural topology optimization: A review. *Struct Multidiscip Optim* 2013; **48**:437–72. doi:10.1007/s00158-013-0912-y.

[6] Sigmund O, Maute K. Topology optimization approaches: A comparative review. *Struct Multidiscip Optim* 2013; **48**:1031–55. doi:10.1007/s00158-013-0978-6.

[7] Suresh K, Turevsky I. Efficient generation of pareto-optimal topologies for compliance optimization. *Int J Numer Methods Eng* 2011; **87**:1207–28. doi:10.1002/nme.3165.

[8] Suresh K. Efficient Generation of Large-Scale Pareto-Optimal Topologies. *Struct Multidiscip Optim* 2013; **47**:49–61. doi:10.1007/s00158-012-0807-3.

[9] Zhou S, Wang MY. Multimaterial structural topology optimization with a generalized Cahn-Hilliard model of multiphase transition. *Struct Multidiscip Optim* 2007; **33**:89–111. doi:10.1007/s00158-006-0035-9.

[10] Zhou S, Wang MY. 3D Multi-Material Structural Topology Optimization with the Generalized Cahn-Hilliard Equations. *C Comput Model Eng Sci* n.d.; **16**:83–102. doi:10.3970/cmes.2006.016.083.

[11] Tavakoli R. Multimaterial topology optimization by volume constrained Allen–Cahn system and regularized projected steepest descent method. *Comput Methods Appl Mech Eng* 2014; **276**:534–65. doi:10.1016/j.cma.2014.04.005.

[12] Wang MY, Zhou S. Synthesis of shape and topology of multi-material structures with a phase-field method. *J Comput Mater Des* 2005; **11**:117–38. doi:10.1007/s10820-005-3169-y.

[13] Tavakoli R, Mohseni SM. Alternating active-phase algorithm for multimaterial topology optimization problems: A 115-line MATLAB implementation. *Struct Multidiscip Optim* 2014; **49**:621–42. doi:10.1007/s00158-013-0999-1.

[14] Huang X, Xie YM. Bi-directional evolutionary topology optimization of continuum structures with one or multiple materials. *Comput Mech* 2009; **43**:393–401. doi:10.1007/s00466-008-0312-0.

[15] Sigmund O, Torquato S. Design of materials with extreme thermal expansion using a three-phase topology optimization method. *J Mech Phys Solids* 1997; **45**:1037–67. doi:10.1016/S0022-5096(96)00114-7.

[16] Sigmund O. Design of multiphysics actuators using topology optimization - Part II: Two-material structures. *Comput Methods Appl Mech Eng* 2001; **190**:6605–27. doi:10.1016/S0045-7825(01)00252-3.

[17] Gibiansky L V., Sigmund O. Multiphase composites with extremal bulk modulus. *J Mech Phys Solids* 2000; **48**:461–98. doi:10.1016/S0022-5096(99)00043-5.

[18] Bendsøe MP, Sigmund O. Material interpolation schemes in topology optimization. *Arch Appl Mech* 1999; **69**:635–54. doi:10.1007/s004190050248.

[19] Yin L, Ananthasuresh GK. Topology optimization of compliant mechanisms with multiple materials using a peak function material interpolation scheme. *Struct Multidiscip Optim* 2001; **23**:49–62. doi:10.1007/s00158-001-0165-z.

[20] Gao T, Zhang W. A mass constraint formulation for structural topology optimization with multiphase materials. *Int J Numer Methods Eng* 2011; **88**:774–96. doi:10.1002/nme.3197.

[21] Hvejsel CF, Lund E. Material interpolation schemes for unified topology and multi-material optimization. *Struct Multidiscip Optim* 2011; **43**:811–25. doi:10.1007/s00158-011-0625-z.

[22] Stegmann J, Lund E. Discrete material optimization of general composite shell structures. *Int J Numer Methods Eng* 2005; **62**:2009–27. doi:10.1002/nme.1259.

[23] Park J, Sutradhar A. A multi-resolution method for 3D multi-material topology optimization. *Comput Methods Appl Mech Eng* 2015; **285**:571–86. doi:10.1016/j.cma.2014.10.011.

[24] Xia Q, Wang MY. Simultaneous optimization of the material properties and the topology of functionally graded structures. *CAD Comput Aided Des* 2008; **40**:660–75. doi:10.1016/j.cad.2008.01.014.

[25] Taheri AH, Hassani B, Moghaddam NZ. Thermo-elastic optimization of material distribution of functionally graded structures by an isogeometrical approach. *Int J Solids Struct* 2014; **51**:416–29. doi:10.1016/j.ijsolstr.2013.10.014.

[26] Carbonari RC, Paulino GH, Silva ECN. Integral Piezoactuator System with Optimum Placement of Functionally Graded Material -- A Topology Optimization Paradigm. *J Intell Mater Syst Struct* 2010; **21**:1653–68. doi:10.1177/1045389X10386129.

[27] Carbonari RC, Silva ECN, Paulino GH. Topology optimization design of functionally graded bimorph-type piezoelectric actuators. *Smart Mater Struct* 2007; **16**:2605–20. doi:10.1088/0964-1726/16/6/065.

[28] Carbonari1 RC, Silva ECN, Paulino GH. Multi-actuated functionally graded piezoelectricmicro-tools design:Amultiphysics topology optimization approach. *Int J Numer Methods Eng* 2009; **77**:301–36. doi:10.1002/nme.2403.

[29] Vatanabe SL, Paulino GH, Silva ECN. Design of functionally graded piezocomposites using topology optimization and homogenization - Toward effective energy harvesting materials. *Comput Methods Appl Mech Eng* 2013; **266**:205–18. doi:10.1016/j.cma.2013.07.003.

[30] Paulino GH, Silva ECN. Design of Functionally Graded Structures Using Topology Optimization. *Mater Sci Forum* 2005; **492-493**:435–40. doi:10.4028/www.scientific.net/MSF.492-493.435.

[31] Almeida SRM, Paulino GH, Silva ECN. Layout and material gradation in topology optimization of functionally graded structures: A global-local approach. *Struct Multidiscip Optim* 2010; **42**:855–68. doi:10.1007/s00158-010-0514-x.

[32] Radman A, Huang X, Xie YM. Topology optimization of functionally graded cellular materials. *J Mater Sci* 2012:1503–10. doi:10.1007/s10853-012-6905-1.

[33] Jebeli SM, Panahi MS. An evolutionary approach for simultaneous optimization of material property distribution and topology of FG structures. *Int J Comput Eng Softw* 2015; **32**:234–57. doi:http://dx.doi.org/10.1108/EC-07-2013-0188.

[34] Koo B, Ha S-H, Kim H-S, Cho S. Isogeometric Shape Design Optimization of Geometrically Nonlinear Structures. *Mech Based Des Struct Mach* 2013; **41**:337–58. doi:10.1080/15397734.2012.750226.

[35] Qian X. Full analytical sensitivities in NURBS based isogeometric shape optimization. *Comput Methods Appl Mech Eng* 2010; **199**:2059–71. doi:10.1016/j.cma.2010.03.005.

[36] Azegami H, Fukumoto S, Aoyama T. Shape optimization of continua using NURBS as basis functions. *Struct Multidiscip Optim* 2013; **47**:247–58. doi:10.1007/s00158-012-0822-4.

[37] Manh ND, Evgrafov A, Gersborg AR, Gravesen J. Isogeometric shape optimization of vibrating membranes. *Comput Methods Appl Mech Eng* 2011; **200**:1343–53. doi:10.1016/j.cma.2010.12.015.

[38] Hassani B, Tavakkoli SM, Moghadam NZ. Application of isogeometric analysis in structural shape optimization. *Sci Iran* 2011; **18**:846–52. doi:10.1016/j.scient.2011.07.014.

[39] Cho S, Ha SH. Isogeometric shape design optimization: Exact geometry and enhanced sensitivity. *Struct Multidiscip Optim* 2009; **38**:53–70. doi:10.1007/s00158-008-0266-z.

[40] Wall WA, Frenzel MA, Cyron C. Isogeometric structural shape optimization. *Comput Methods Appl Mech Eng* 2008; **197**:2976–88. doi:10.1016/j.cma.2008.01.025.

[41] Taheri AH, Hassani B. Simultaneous isogeometrical shape and material design of functionally graded structures for optimal eigenfrequencies. *Comput Methods Appl Mech Eng* 2014; **277**:46–80. doi:10.1016/j.cma.2014.04.014.

[42] Kim HJ, Seo YD, Youn SK. Isogeometric analysis with trimming technique for problems of arbitrary complex topology. *Comput Methods Appl Mech Eng* 2010; **199**:2796–812. doi:10.1016/j.cma.2010.04.015.

[43] Seo YD, Kim HJ, Youn SK. Isogeometric topology optimization using trimmed spline surfaces. *Comput Methods Appl Mech Eng* 2010; **199**:3270–96. doi:10.1016/j.cma.2010.06.033.

[44] Seo YD, Kim HJ, Youn SK. Shape optimization and its extension to topological design based on isogeometric analysis. *Int J Solids Struct* 2010; **47**:1618–40. doi:10.1016/j.ijsolstr.2010.03.004.

[45] Dedè L, Borden MMJ, Hughes TJRT. Isogeometric analysis for topology optimization with a phase field model. *Arch Comput Methods Eng* 2012; **19**:427–65. doi:10.1007/s11831-012-9075-z.

[46] Tavakkoli SM, Hassani B. Isogeometric Topology Optimization by Using Optimality Criteria and Implicit Function. *Int J Optim Civ Eng* 2014; **4**:151–63.

[47] Hassani B, Khanzadi M, Tavakkoli SM. An isogeometrical approach to structural topology optimization by optimality criteria. *Struct Multidiscip Optim* 2012; **45**:223–33. doi:10.1007/s00158-011-0680-5.

[48] Qian X. Topology optimization in B-spline space. *Comput Methods Appl Mech Eng* 2013; **265**:15–35. doi:10.1016/j.cma.2013.06.001.

[49] Shojaee S, Mohamadian M, Valizadeh N. Composition of Isogeometric Analysis With Level Set Method for Structural Topology Optimization. *Int J Optim Civ Eng* 2012; **2**:47–70.

[50] Wang M, Qian X. Efficient Filtering in Topology. *J Mech Des* 2015; **137**:1–10. doi:10.1115/1.4029373.

[51] Nagy AP, Ijsselmuiden ST, Abdalla MM. Isogeometric design of anisotropic shells: Optimal form and material distribution. *Comput Methods Appl Mech Eng* 2013; **264**:145–62. doi:10.1016/j.cma.2013.05.019.

[52] Hassani B, Taheri AH, Moghaddam NZ. An improved isogeometrical analysis approach to functionally graded plane elasticity problems. *Appl Math Model* 2013; **37**:9242–68. doi:10.1016/j.apm.2013.04.048.

[53] Taheri AH, Abolbashari MH, Hassani B. Free vibration characteristics of functionally graded structures by an isogeometrical analysis approach. *Proc Inst Mech Eng Part C J Mech Eng Sci* 2014; **228**:1512–30. doi:10.1177/0954406213508757.

[54] Borrvall T. Topology Optimization of Elastic Continua Using Restriction. *Arch Comput Methods Eng* 2001; **8**:351–85. doi:10.1007/BF02743737.

[55] Mirzendehdel AM, Suresh K. Multi-Material Topology Optimization for Additive Manufacturing. *J Mech Des* 2015; **137**:1–12. doi:10.1115/1.4031088.

[56] Matsui K, Terada K. Continuous approximation of material distribution for topology optimization. *Int J Numer Methods Eng* 2004; **59**:1925–44. doi:10.1002/nme.945.

[57] Bendsoe MP, Sigmund O. Topology Optimization: Theory, Methods and Applications. Springer Science & Business Media; 2003.

[58] Petersson J, Sigmund O. Slope constrained topology optimization. *Int J Numer Methods Eng* 1998; **41**:1417–34. doi:10.1002/(SICI)1097-0207(19980430)41:8<1417::AID-NME344>3.0.CO;2-N.

[59] Bourdin B. Filters in topology optimization. *Int J Numer Methods Eng* 2001; **50**:2143–58. doi:10.1002/nme.116.

[60] Sigmund O. Morphology-based black and white filters for topology optimization. *Struct Multidiscip Optim* 2007; **33**:401–24. doi:10.1007/s00158-006-0087-x.

[61] Poulsen TA. A new scheme for imposing a minimum length scale in topology optimization. *Int J Numer Methods Eng* 2003; **57**:741–60. doi:10.1002/nme.694.

[62] Ambrosio L, Buttazzo G. An optimal design problem with perimeter penalization. *Calc Var Partial Differ Equ* 1993; **1**:55–69. doi:10.1007/BF02163264.

[63] Petersson J. Some convergence results in perimeter-controlled topology optimization. *Comput Methods Appl Mech Eng* 1999; **171**:123–40. doi:10.1016/S0045-7825(98)00248-5.

[64] Haber RB, Jog CS, Bendsoe MP. A new approach to variable-topology shape design using a constraint on perimeter. *Struct Optim* 1996; **11**:1–12. doi:10.1007/BF01279647.

[65] Guest JK. Topology optimization with multiple phase projection. *Comput Methods Appl Mech Eng* 2009; **199**:123–35. doi:10.1016/j.cma.2009.09.023.

[66] Zhang W, Zhong W, Guo X. An explicit length scale control approach in SIMP-based topology optimization. *Comput Methods Appl Mech Eng* 2014; **282**:71–86. doi:10.1016/j.cma.2014.08.027.

[67] Hashin Z, Shtrikman S. A variational approach to the theory of the elastic behaviour of polycrystals. *J Mech Phys Solids* 1962; **10**:343–52. doi:10.1016/0022-5096(62)90005-4.

[68] Svanberg K. The method of moving asymptotes—a new method for structural optimization. *Int J Numer Methods Eng* 1987; **24**:359–73. doi:10.1002/nme.1620240207.

[69] Kou XY, Parks GT, Tan ST. Optimal design of functionally graded materials using a procedural model and particle swarm optimization. *Comput Des* 2012; **44**:300–10. doi:10.1016/j.cad.2011.10.007.

[70] Goupee AJ, Vel SS. Optimization of natural frequencies of bidirectional functionally graded beams. *Struct Multidiscip Optim* 2006; **32**:473–84. doi:10.1007/s00158-006-0022-1.

Figure Captions

Figure 1. Configuration of the L-bracket with a unit load at the end.

Figure 2. Optimization results for the L-bracket with the overall mass constraint $\bar{M} = 30 \times 10^3\ kg$: (a) single material $M1$, (b) single material $M2$, and (c) multi-material $M1 \& M2$.

Figure 3. Volume fraction of material phases in the optimal designs.

Figure 4. Multi-material design of the L-bracket subjected to different mass constraints (*kg*) of (a) $\bar{M} = 20 \times 10^3$, (b) $\bar{M} = 40 \times 10^3$, (c) $\bar{M} = 50 \times 10^3$ and (d) $\bar{M} = 70 \times 10^3$.

Figure 5. Comparison of the compliance of multi-material designs with single material cases for different mass constraints.

Figure 6. The simply supported MBB beam with a unit load on the top center.

Figure 7. Optimum designs for different selections of perimeter control parameters (a) case 1, (b) case 2, (c) case 3 and (d) case 4.

Figure 8. Geometry and boundary conditions of the quarter annulus.

Figure 9. Optimal single material design of the quarter annulus.

Figure 10. Multi-material optimal designs of the annulus with different meshes of (a) 98×40, (b) 140×58 and (c) 175×73 elements.

Figure 11. Geometry and boundary conditions of the bridge-type structure.

Figure 12. Distribution of the strong phase (E_1) within the optimal topologies of the FGM bridge for different perimeter control coefficients: (a) case 1, (b) case 2, (c) case (3), and (d) case 4.

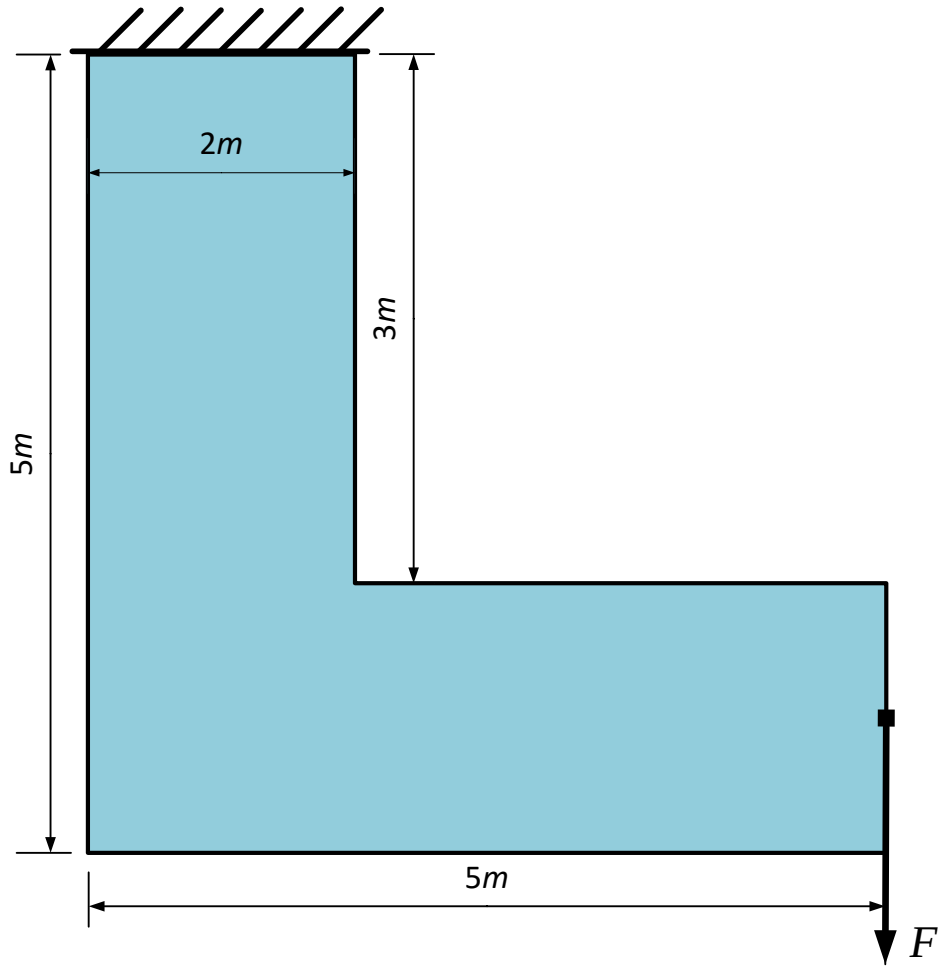

Figure 1. Configuration of the L-bracket with a unit load at the end.

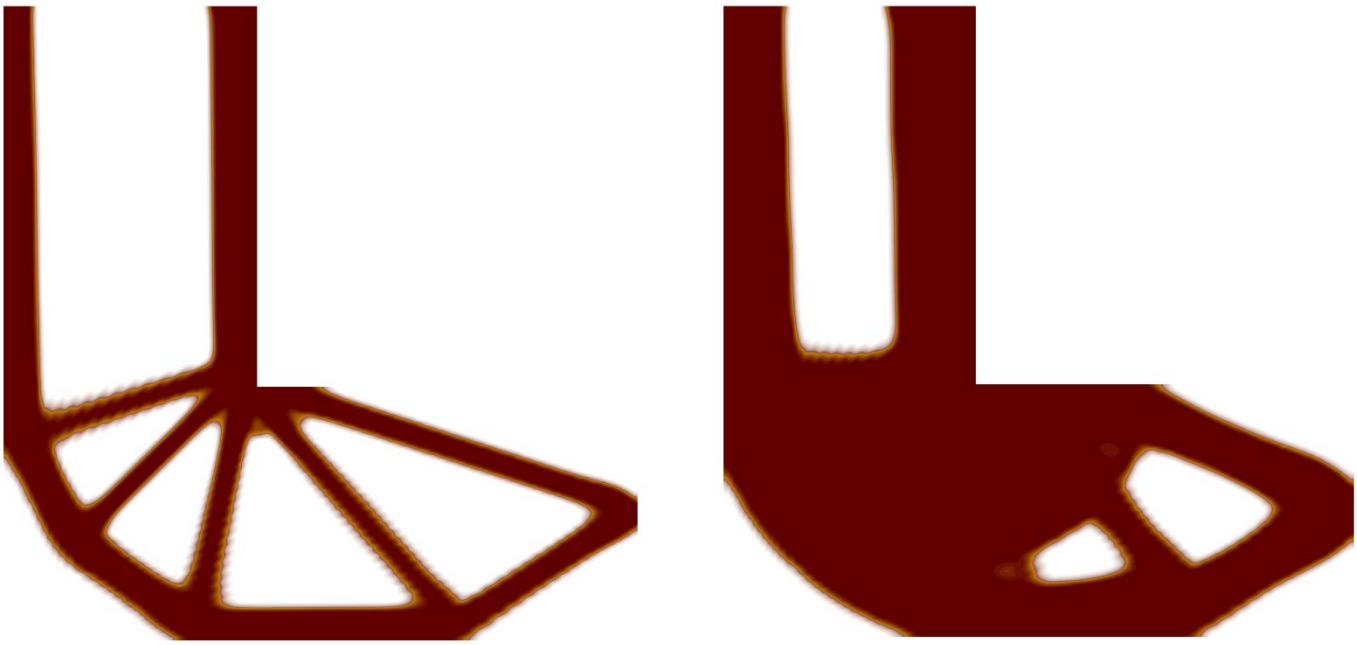

(a) **(b)**

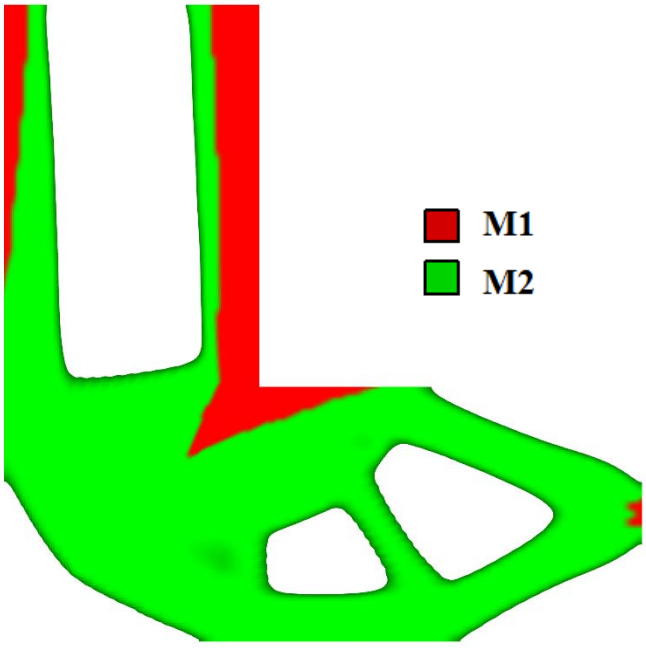

(c)

Figure 2. Optimization results for the L-bracket with the overall mass constraint $\bar{M} = 30 \times 10^3\ kg$: (a) single material $M1$, (b) single material $M2$, and (c) multi-material $M1 \& M2$.

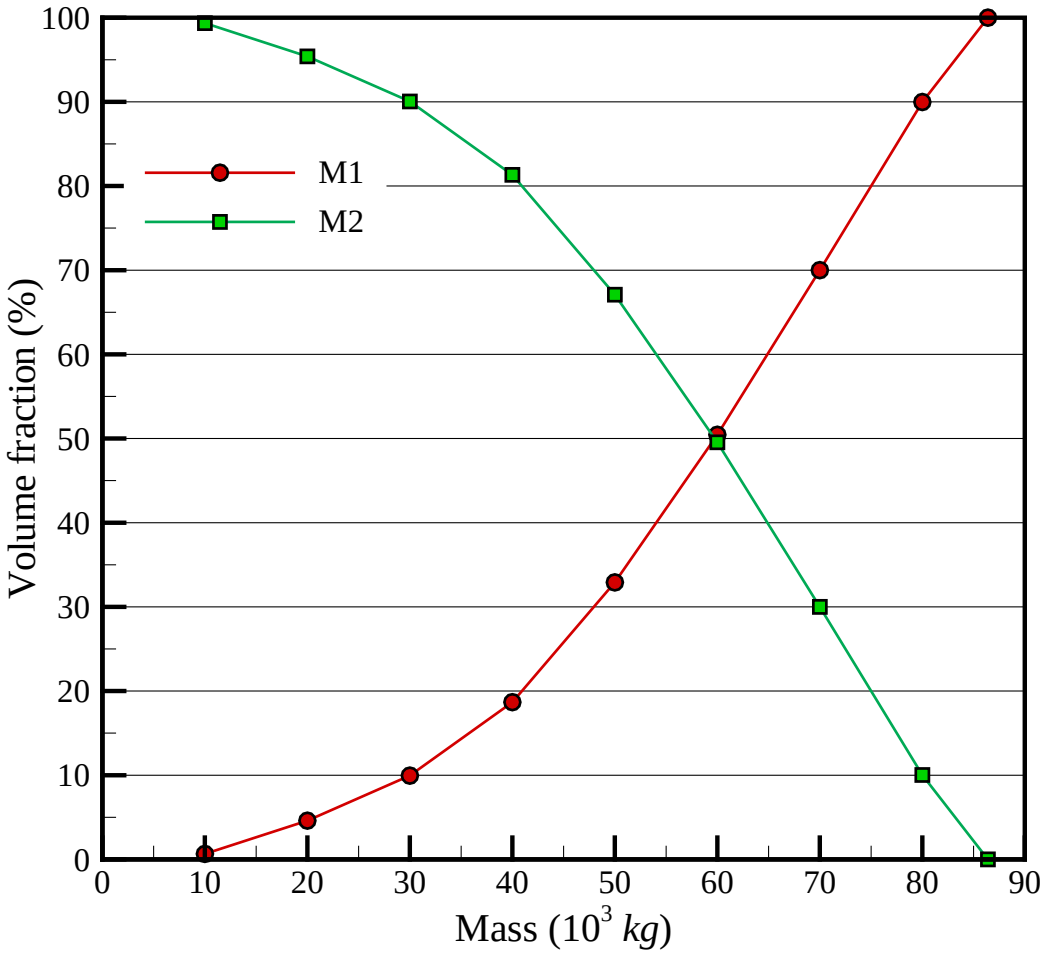

Figure 3. Volume fraction of material phases in the optimal designs.

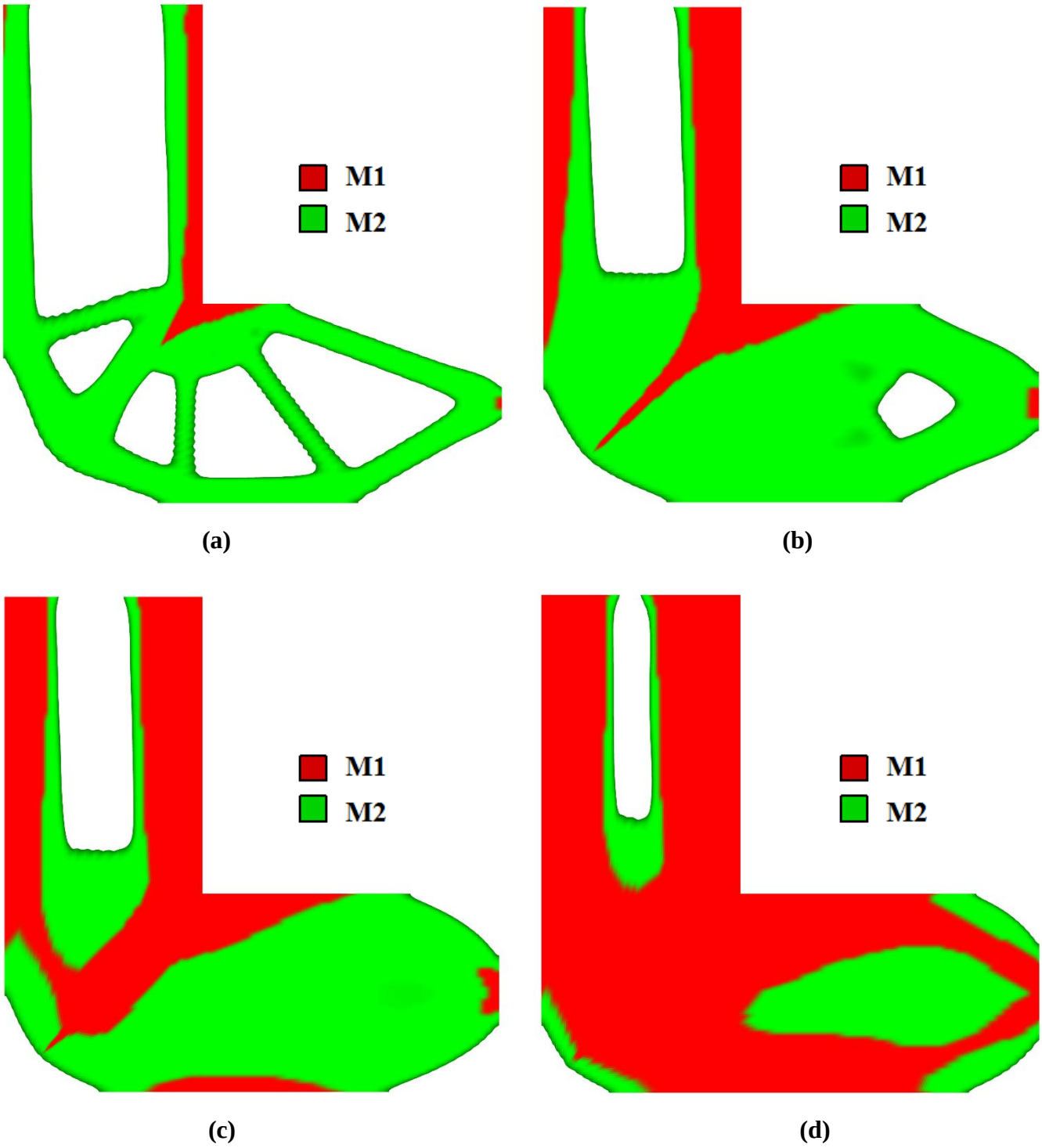

Figure 4. Multi-material design of the L-bracket subjected to different mass constraints (*kg*) of (a) $\bar{M} = 20\times10^3$, (b) $\bar{M} = 40\times10^3$, (c) $\bar{M} = 50\times10^3$ and (d) $\bar{M} = 70\times10^3$.

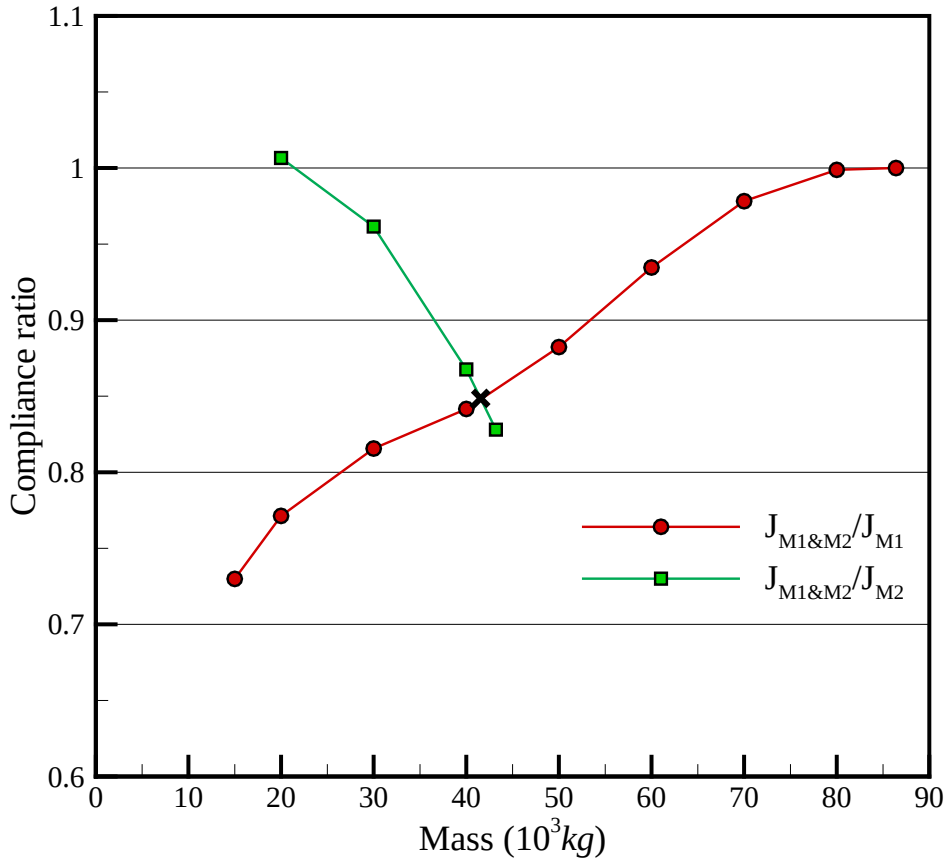

Figure 5. Comparison of the compliance of multi-material designs with single material cases for different mass constraints.

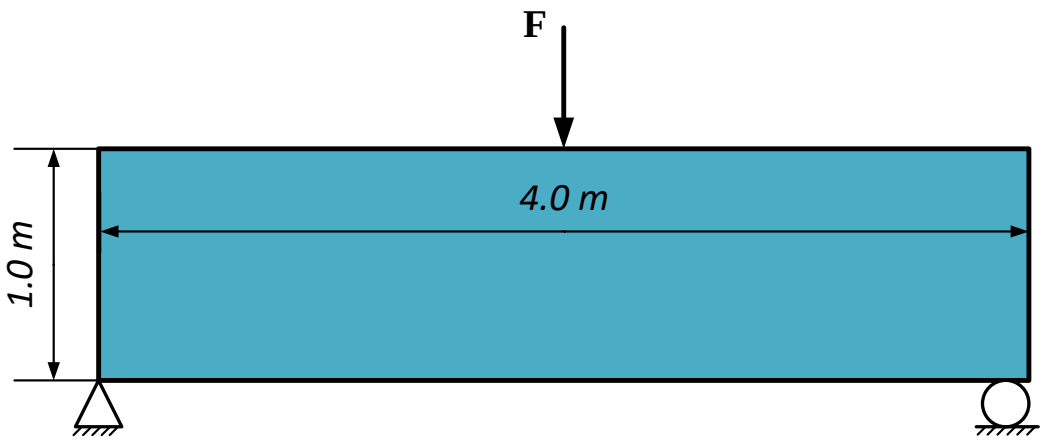

Figure 6. The simply supported MBB beam with a unit load on the top center.

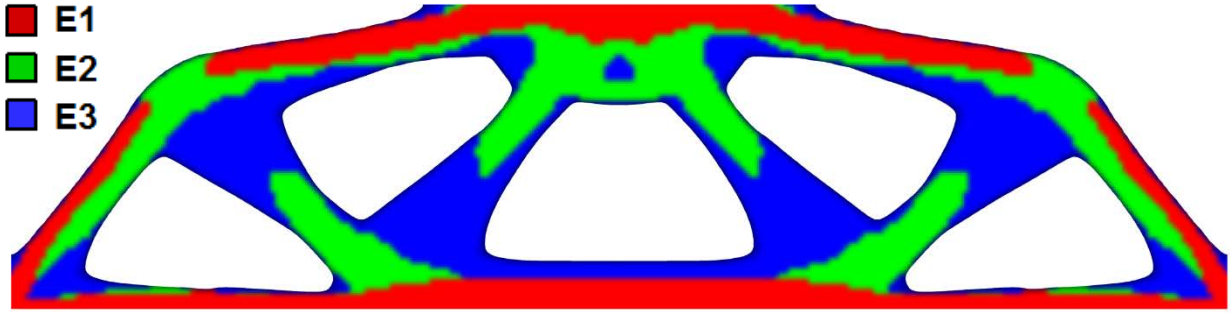

(a)

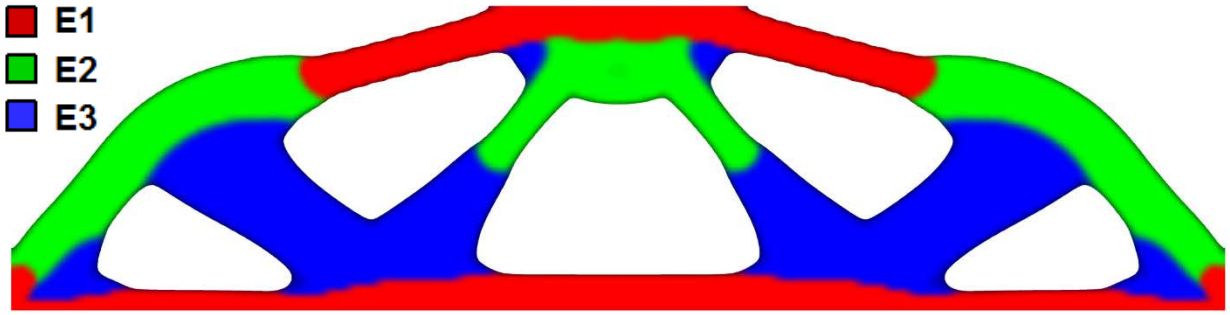

(b)

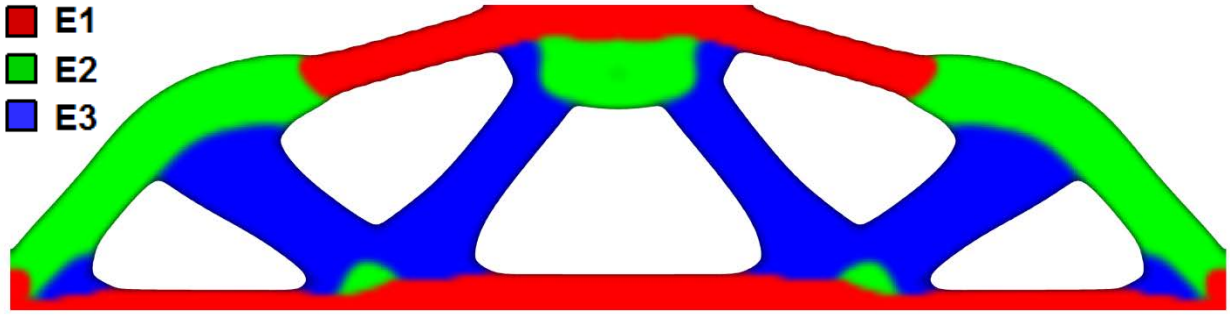

(c)

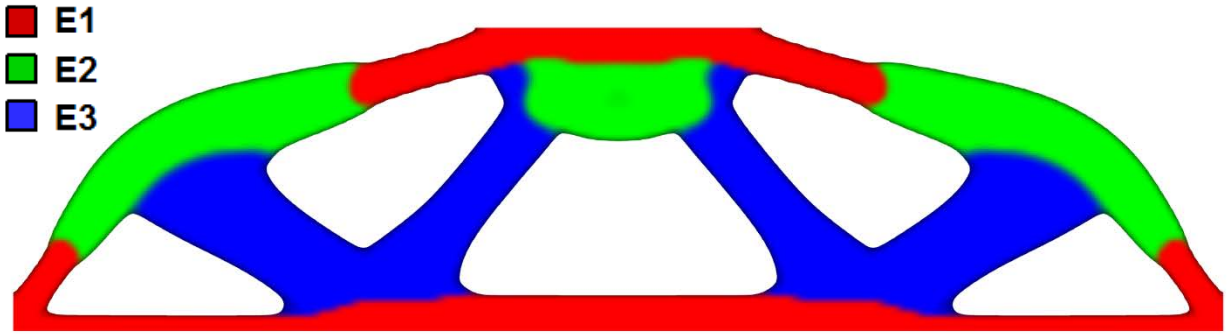

(d)

Figure 7. Optimum designs for different selections of perimeter control parameters (a) case 1, (b) case 2, (c) case 3 and (d) case 4.

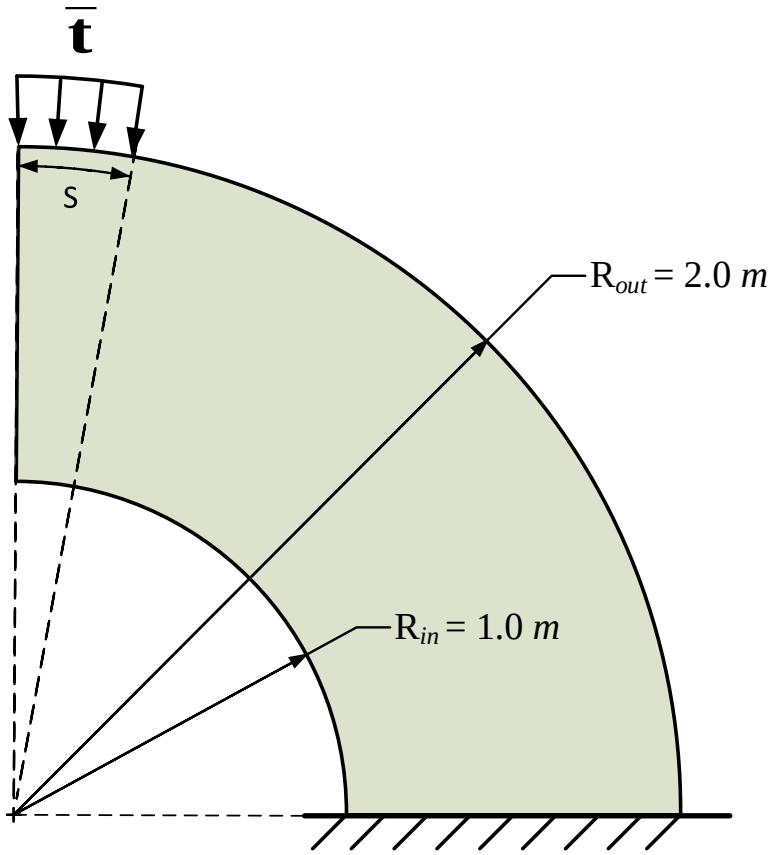

Figure 8. Geometry and boundary conditions of the quarter annulus.

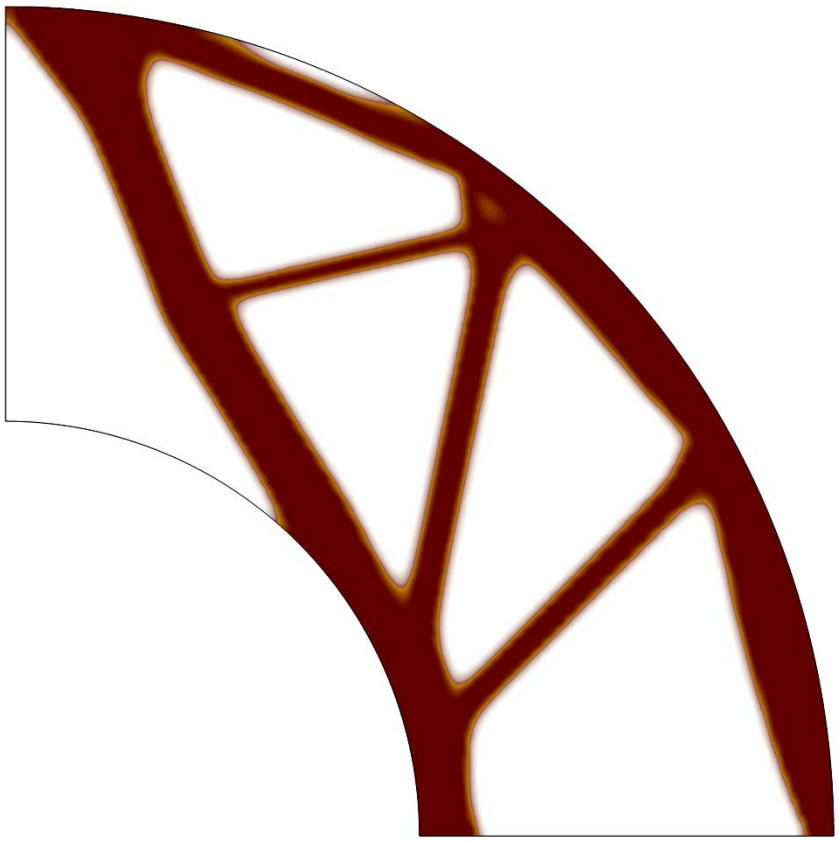

Figure 9. Optimal single material design of the quarter annulus.

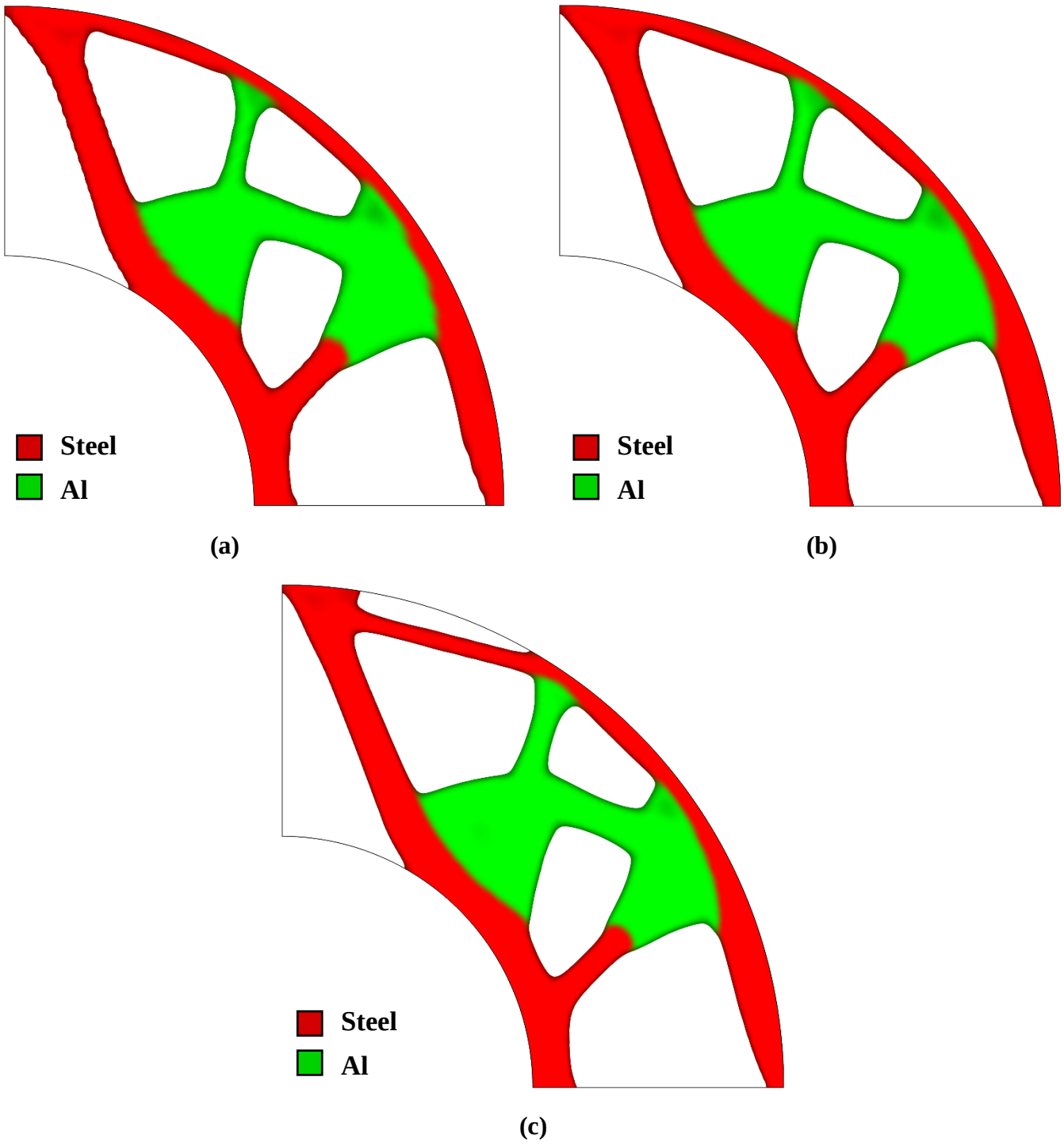

Figure 10. Multi-material optimal designs of the annulus with different meshes of (a) 98×40, (b) 140×58 and (c) 175×73 elements.

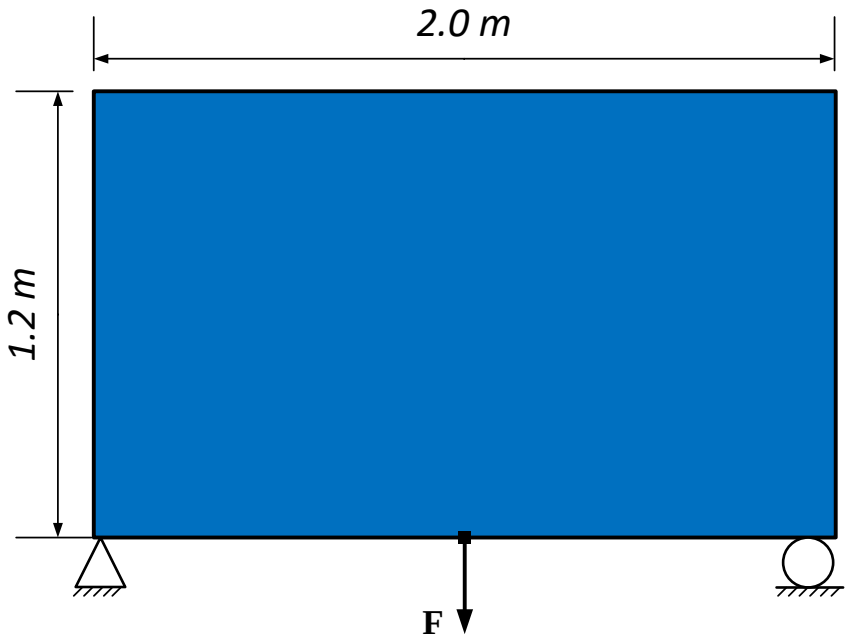

Figure 11. Geometry and boundary conditions of the bridge-type structure.

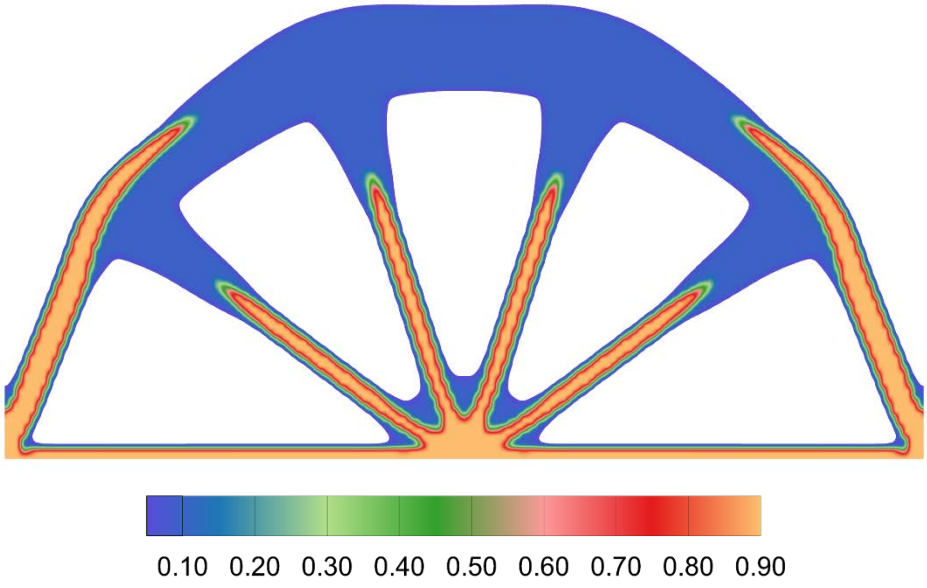
0.10 0.20 0.30 0.40 0.50 0.60 0.70 0.80 0.90

(a)

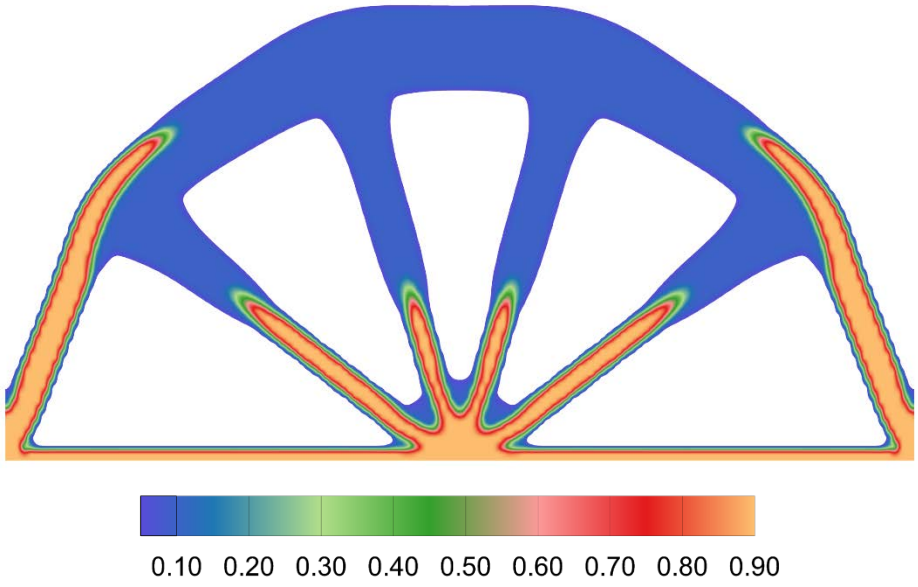
0.10 0.20 0.30 0.40 0.50 0.60 0.70 0.80 0.90

(b)

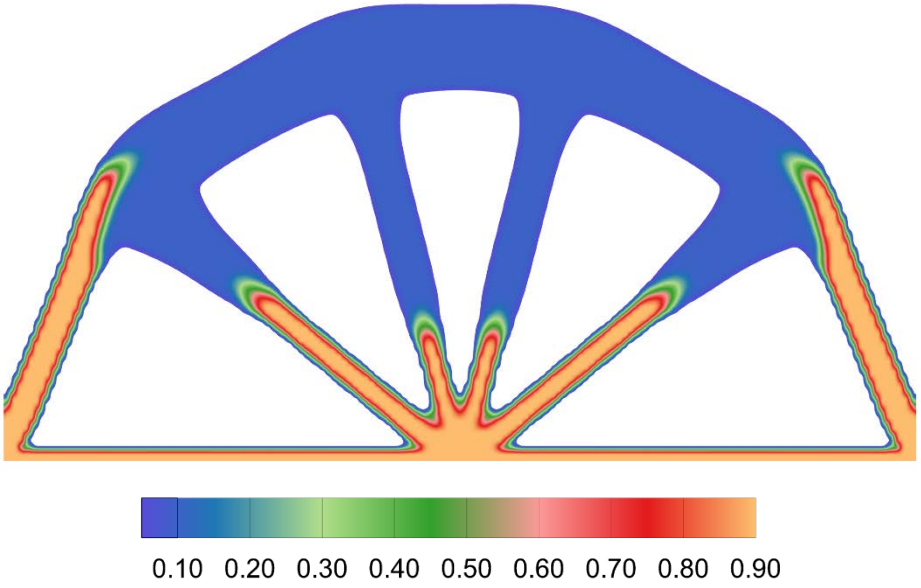

(c)

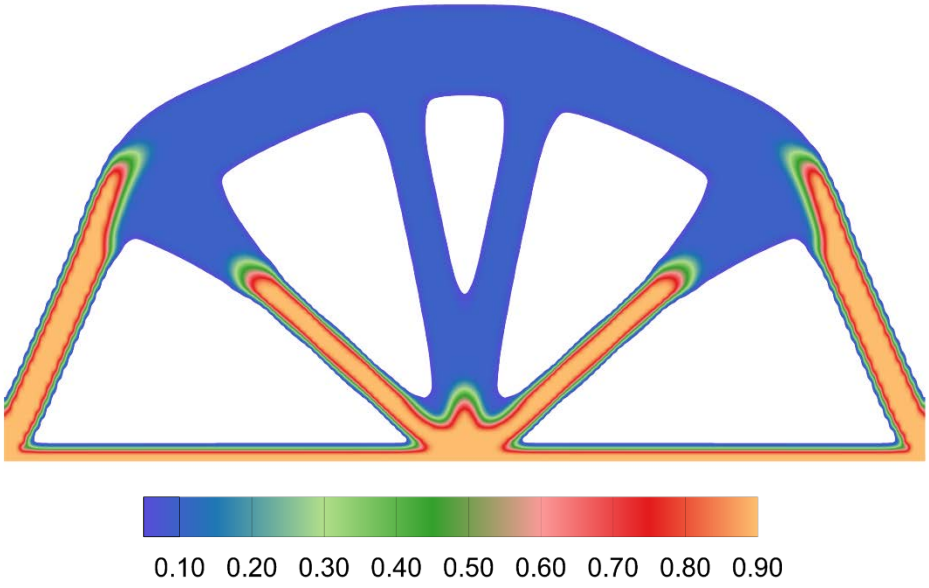

(d)

Figure 12. Distribution of the strong phase (E_1) within the optimal topologies of the FGM bridge for different perimeter control coefficients: (a) case 1, (b) case 2, (c) case (3), and (d) case 4.